The Effect of Tool Pin Size and Taper Angle on the Thermal Process and Plastic Material Flow in Friction Stir Welding

Jie Chen
MOE Key Lab for Liquid-Solid Structure Evolution and Materials Processing, Institute of Materials Joining, Shandong University, Jinan, 250061, China

Lei Shi (lei.shi@sdu.edu.cn)
Shandong University https://orcid.org/0000-0002-9831-1872

Chuansong Wu
MOE Key Lab for Liquid-Solid Structure Evolution and Materials Processing, Institute of Materials Joining, Shandong University, Jinan, 250061, China

Yuanning Jiang
MOE Key Lab for Liquid-Solid Structure Evolution and Materials Processing, Institute of Materials Joining, Shandong University, Jinan, 250061, China

---

Research Article

Keywords: Friction stir welding (FSW), Numerical simulation, Tool pin size, Thermal process, Plastic material flow

Posted Date: March 24th, 2021

DOI: https://doi.org/10.21203/rs.3.rs-335152/v1

Version of Record: A version of this preprint was published at The International Journal of Advanced Manufacturing Technology on July 12th, 2021. See the published version at https://doi.org/10.1007/s00170-021-07650-x.

The effect of tool pin size and taper angle on the thermal process and plastic material flow in friction stir welding

Jie Chen, Lei Shi *, Chuansong Wu, Yuanning Jiang

MOE Key Lab for Liquid-Solid Structure Evolution and Materials Processing, Institute of Materials Joining, Shandong University, Jinan, 250061, China

* Corresponding author, E-mail: lei.shi@sdu.edu.cn

Abstract: Friction stir welding (FSW) tool pin, as a critical component of FSW tool, plays an important role in determining the final joint properties by affecting the heat generation, plastic material flow, welding loads and so on. However, the influence of tool pin on heat and mass transfer in FSW are not elucidated. In the present study, a validated model was adopted to quantitatively analyze the effects of pin size and taper angle on the thermal process and plastic material flow in FSW. It reveals that the torque and transverse force imposed on the pin are increased with the increase of the pin diameters (including its root diameter, its tip diameter and its size in condition of constant taper angle), while the total tool torque various a little for the tool pin diameter considered in this study. When the pin diameters increase, the viscosity of the materials near the pin is decreased, while the temperature as well as the flow velocity is increased. More plastic material near the tool could rotate around the tool with an increase of the pin diameter. The TMAZ boundary is enlarged with larger pin diameters in FSW. Particularly, the shear layer thickness of the same horizontal plane in the range of 1 mm < z < 5 mm is significantly enlarged with an increase of pin root diameters. However, the shear layer thickness of the same horizontal plane in the region of z < 5 mm is increased when using a larger pin tip diameter. In addition, maximum width of TMAZ boundary at the top surface of workpiece was not affected by pin diameters. The model is validated by experimental results. It lays solid foundation for optimizing the tool pin size and taper angle in FSW.

Keywords: Friction stir welding (FSW); Numerical simulation; Tool pin size; Thermal process; Plastic material flow

1. Introduction

As a solid-state joining technology, friction stir welding (FSW) technology can avoid hot cracks, pores and other problems in fusion welding, and has prominent advantages in the welding of aluminum, magnesium and other lightweight alloys [1,2]. In FSW process, the heat is provided by the friction heat generation between the tool and the workpiece and the plastic deformation of the shear layer inside the material [3,4]. As an important part of FSW equipment, the tool is composed of shoulder and pin, which plays an important role in obtaining good welding joint performance [5,6].

The role of tool pin in FSW is to drive the material flow and provide part of heat. A large number of experimental studies have shown that the shape and size of the pin will affect the thermal cycles, material flow behaviors and welding loads in FSW, and determine the final joint properties [7-9]. Elangovan et al. experimentally studied the effects of pin shape (straight cylinder, tapered cylinder, threaded cylinder, triangle and square) and shoulder diameters on the joint formation and mechanical property. They obtained defect-free welds with the best mechanical properties when using a square pin with a shoulder diameter of 18 mm [10]. Marzbanrad et al. studied the influence of pin profile on mechanical properties and microstructure of AA5083 friction stir welded joint. They revealed that the mechanical property of joint produced by a square pin is higher than the one by a cylindrical pin [11]. Prakash et al. numerically studied the effects of pin profiles on the welding zone shape in FSW by comparing four kinds of pin profiles, including cylindrical, conical, cylindrical-conical and stepped-conical. It is found that the welding zone shape produced by the stepped-conical pin is the vase shape dominated by cylinder, while the ones produced by the other pins is the vase shape dominated by basin [12]. Su et al. quantitatively analyzed the thermo-physical phenomena in FSW of axisymmetrical conical pin and asymmetrical triflat pin using CFD techniques. It is found that the "stirring action" of the asymmetric triflat pin is more intense and the deformation region is larger [13].

All the above studies show that the geometry of the pin has an important influence on the FSW process. However, the size of pin also has a major impact on

the thermal process and plastic material flow behaviors in FSW. Akbari et al. studied the effect of cylindrical pin diameter on the axial force and transverse force as well as the welding temperature. The results showed that the axial force, transverse force and peak temperature are all increased with an increase of the pin diameter [14]. Kulekci et al. studied the effect of cylindrical pin diameter on the fatigue behavior of FSW lap joint. They found that a larger pin diameter would reduce the fatigue strength of the joint when the welding parameters were kept constants [15]. Ramachandran et al. found that taper angle of the pin significantly affects the thickness and composition of the intermetallic compound layer, as well as the joint properties during friction stir welding of aluminum alloy to HSLA steel [16]. Zhang et al. used the thermal-mechanical coupling model to study the effect of the taper angle of the pin on the thermal process in FSW. They found that the peak temperature and the fluidity of surrounding materials are increased when the taper angle increased [17]. Buffa et al. found that an increase of the pin taper angle could expand the heat affected zone and thermal-mechanical affected zone. In addition, they also found that a larger pin taper angle can lead to a more uniform temperature distribution along the thickness of the plate, which is conducive to reducing welding deformation [18].

The tool pin size and its taper angle play a major role in determining the thermal process and plastic material flow. However, the effects of the pin size, especially its root and tip diameter on the thermal process and plastic material flow behaviors are not revealed. In this paper, a validated model was used to quantitatively study the effect of pin size and its taper angle on the thermal processes in FSW. The thermal field and plastic material flow behaviors for different pin size and taper angle have been systematically analyzed. It lays solid foundation for optimizing the tool pin size and taper angle in FSW.

2. Experimental procedures

Fig. 1 shows the schematic drawing of FSW process. 2024-T3 aluminum alloy plate of 6 mm thickness was used as the base materials, and its chemical composition was shown in Table 1. The tool is composed of a shoulder and a pin (as shown in Fig.

2). The diameter of the shoulder is 15 mm. Different pin root diameter (PRD) and pin tip diameter (PTD) are used, and the length of the pin is kept a constant as 5.7 mm. The FSW tool is made of H13 steel. During the welding process, the tool inclination angle is 2.5° with respected to z axis. The welding thermal cycles were measured by K-type thermocouples. The measured point was located at advancing side (AS) 3 mm from the upper surface of the weld, and 10 mm and 20 mm from the center line of the weld, respectively. The sample was finished with emery papers, polished and etched, and then the macroscopic morphology of the weld was observed by optical microscope.

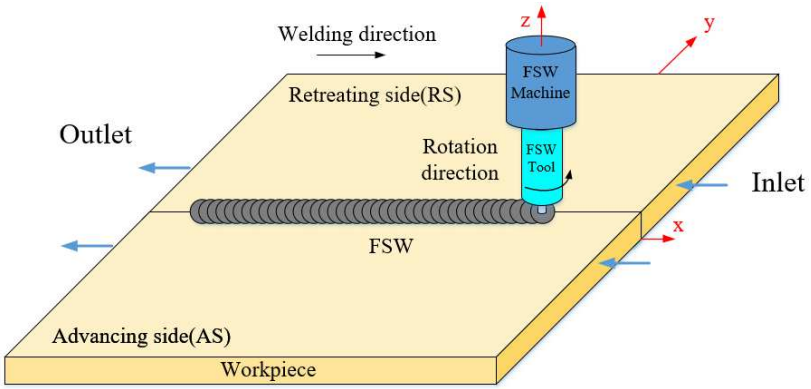

Fig. 1. Schematic drawing of the friction stir welding (FSW) process.

Table 1 Chemical compositions of 2024-T3 aluminum alloy

Element	Si	Fe	Cu	Mn	Mg	Ni	Zn	Ti	Al
Mass fraction/%	0.15	0.25	4.58	0.63	1.59	<0.10	0.20	<0.10	Bal

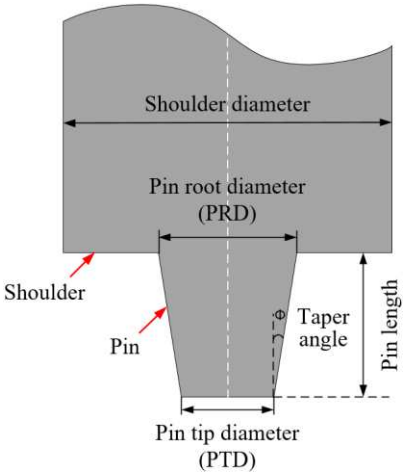

Fig. 2. Schematic drawing of the tool geometry.

3. Modeling approaches

Commercial CFD software ANSYS Fluent was used to simulate the model. The Semi-Implicit method was used to solve the continuity equation, momentum conservation equation and energy conservation equation. In the model, the workpiece material is regarded as a non-Newtonian incompressible continuous fluid [19]. The tool is assumed as a rigid body and not included in the model [20]. The contact interfaces between the tool and the workpiece are treated as moving walls.

3.1 Geometry description

In the FSW model, the calculation area of the workpiece was $500 \times 300 \times 6$ mm^3 (length × width × height). The diameter of tool shoulder was kept as 15 mm, and the length of the pin was 5.7 mm. The effects of pin root diameter were studied, in which the pin tip diameter was kept as 3.2 mm while its root diameters were 3.2 mm, 4.4 mm and 5.6 mm respectively. The effects of pin tip diameter were studied by keeping the pin root diameter as 5.6 mm and its tip diameters were chosen as 3.2 mm, 4.4 mm and 5.6 mm, respectively. The effects of pin size in condition of certain taper angle ($\Phi = 12°$) were studied, in which the pin root diameters were 3.2 mm, 4.4 mm and 5.6 mm, and its corresponding tip diameters were 2.6 mm, 3.2 mm and 3.8 mm.

3.2 Material properties

The density of 2024-T3 aluminum alloy is 2780 kg/m^3. The heat capacity and thermal conductivity of the material at different temperatures are respectively calculated as [21],

$$C_p = 0.5417T + 706.9 \ \left(J \cdot kg^{-1} \cdot K^{-1}\right) \quad (1)$$

$$k = 0.0947T + 102.5 \ \left(W \cdot m^{-1} \cdot K^{-1}\right) \quad (2)$$

For non-Newtonian fluids, the relationship between material viscosity and flow stress is as follows [22],

$$\mu = \frac{\sigma}{3\bar{\dot{\varepsilon}}} \quad (3)$$

where $\bar{\dot{\varepsilon}}$ is the effective strain rate, σ is the flow stress of the material, which is considered to be related to temperature and effective strain rate of the material [23], it

is calculated as,

$$\sigma = \frac{1}{\alpha} ln \left\{ \left[\frac{\bar{\varepsilon}}{A} exp\left(\frac{Q}{RT}\right) \right]^{\frac{1}{n}} + \left[\left[\frac{\bar{\varepsilon}}{A} exp\left(\frac{Q}{RT}\right) \right]^{\frac{1}{n}} + 1 \right]^{\frac{1}{2}} \right\} \tag{4}$$

where α, A and n are the material constants, R is the gas constant, T is the absolute temperature，Q is the activation energy.

3.3 Boundary conditions

In this model, the material flows into the calculation domain at the speed equal to the welding speed from the Inlet boundary and out of the Outlet boundary after passing through the tool. The top surface, bottom surface and other sides of the workpiece are assumed as no slip boundary. The velocity boundary condition of the interface between the tool and the workpiece is calculated as follows,

$$\begin{cases} V_x = (1-\delta)\omega r \sin\theta \\ V_y = (1-\delta)\omega r \cos\theta \\ V_z = 0 \end{cases} \tag{5}$$

where V_x、V_y、V_z are the velocities in x, y and z directions respectively, ω is the rotation speed of the tool, r is the radial distance from the tool axis, θ is the angle between the radius vector and the welding direction, δ is the slip rate which is summarized by Arora et al. based on the corresponding relationship in cross-wedge rolling as follows [24],

$$\delta = 0.31 \exp\left(\frac{\omega r}{1.87}\right) - 0.026 \tag{6}$$

Heat conduction and radiation heat transfer occur when the top surface of the workpiece is in contact with air. The two sides of the workpiece are in close contact with the welding fixture, and the bottom surface of the workpiece is in close contact with the backing plate. Heat conduction and heat dissipation are the main forms of heat dissipation. The heat transfer coefficients of the top surface, side and bottom surface are assumed to be 30 W/m^2/K, 200 W/m^2/K and 300 W/m^2/K.

3.4 Heat generation model

In the process of FSW, the heat generation mainly includes the friction heat generation and plastic deformation heat generation of the contact interfaces between

the tool and the workpiece, and the viscous dissipation heat of the plastic material near the tool [25, 26]. The heat flux of the shoulder and the pin bottom surface are calculated as [27, 28],

$$q = \left[\eta(1-\delta)\tau_c + \beta\delta\mu_f P_N\right](\omega r - U\sin\theta) \quad (7)$$

The heat flux of the side of the pin is calculated as,

$$q = \left[\eta(1-\delta)\tau_c + \beta\delta\mu_f \sigma_y\right](\omega r - U\sin\theta) \quad (8)$$

where η is the plastic deformational thermal efficiency coefficient, β is the frictional heat conversion efficiency, τ_c is the shear stress of the material, P_N is the axial pressure, σ_y is the yield strength of the material, U is the welding speed, μ_f is the frictional coefficient which is calculated as [24],

$$\mu_f = 0.5\exp(-\delta\omega r) \quad (9)$$

The heat production of viscous dissipation of the plastic material near the tool can be calculated as [29, 30]:

$$S_v = f_m \sigma \bar{\dot{\varepsilon}} \quad (10)$$

where f_m is a constant representing the mixing degree of atoms in the plastic zone.

4. Results and discussion

4.1 Experimental validation

Fig. 3a and Fig. 3b respectively show the thermal cycles at two monitored points. The monitored locations are 10 mm and 20 mm away from the center line of the weld at the advancing side. The experimentally measured and calculated peak temperatures at the location 10 mm away from the joint line are 613 K and 612 K (Fig. 3a), respectively. While the measured and calculated peak temperatures are respectively 511 K and 497 K at the location 20 mm away from the joint line (Fig. 3b). It can be seen that the calculated thermal cycles are generally consistent with the measured results. However, because the temperature measuring point is close to the starting position of welding, there are some differences between them in the initial heating stage. According to the reference [31], the critical value of viscosity equal to 2.5×10^6 Pa·s could represent the boundary of the thermal-mechanical affected zone

(TMAZ). Fig. 4 shows the calculated and measured TMAZ boundary. It can be seen that the calculated and experimental measured results are in good agreement.

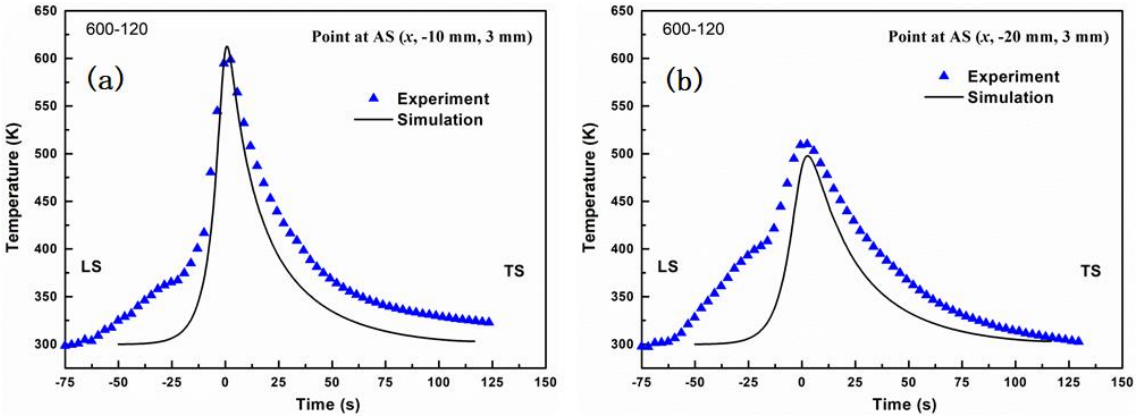

Fig. 3. Calculated and measured thermal cycles at the point (a) 10 mm and (b) 20 mm away from the weld centerline.

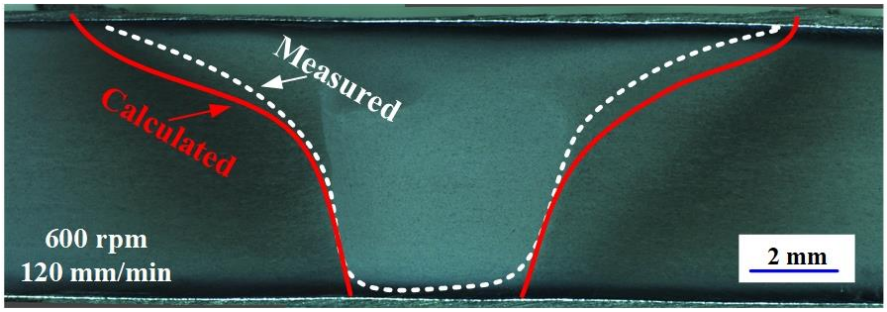

Fig. 4. Calculated and measured TMAZ boundary in weld cross-section.

4.2 The effects of pin root diameter

In this section, the effects of the pin root diameter on the welding thermal process and material flow in FSW are studied. Among them, the pin tip diameter is 3.2 mm and remains unchanged. In this paper, the tool rotation speed and welding speed are designated in brief forms as Rotation-Welding speed. For example, 800-120 represents the case with tool rotation speed of 800 rpm and welding speed of 120 mm/min.

Fig. 5a shows the total tool torque, the torque originated from the pin (i.e., pin torque for short) and the pin torque fraction calculated for different pin root diameters when the rotation speed is 600 rpm and the welding speed is 120 mm/min. It is shown that the increase of PRD has little influence on the total tool torque under the calculated welding conditions. However, when the PRD increases from 3.2 mm to 5.6

mm, the pin torque increases from 2.61 Nm to 4.04 Nm. In addition, the pin torque fraction is increased with an increase of PRD, which is mainly because the contact areas between the pin and the workpiece are increased with an increase of PRD. Fig. 5b presents the total transverse force of the tool calculated for different pin root diameters, as well as the pin transverse force and pin transverse force fraction. As is seen, the total transverse force of the tool is slightly decreased when the PRD increases. It is consistent with the conclusion that the traverse force decreases dramatically for a tool that can stimulate more plastic deformation [32]. In addition, the transverse force originated from the pin and its fractions are dramatically increased with an increase of the pin root diameter.

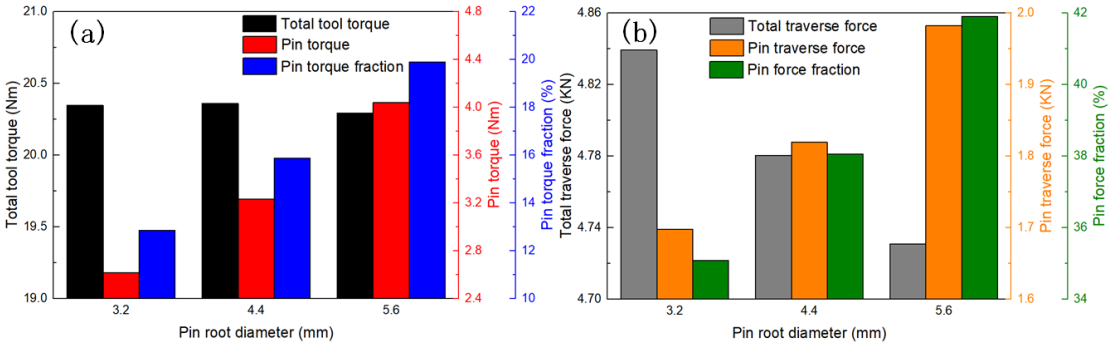

Fig. 5. Comparison of (a) torque and (b) transverse force for different pin root diameters.

Fig. 6 shows the predicted TMAZ boundaries at different PRD (i.e., 3.2 mm, 4.4 mm and 5.6 mm, respectively) for three different welding conditions. By comparing Fig. 6a and Fig. 6b, it can be found that the welding speed has little effect on the TMAZ boundary for the same rotation speed. However, the TMAZ boundary at the PRD of 5.6 mm expands from 6.45 mm to 7.01 mm when the rotation speed increases from 600 rpm to 800 rpm as shown in Fig. 6a and Fig. 6c. This is because the rotation speed significant influence the heat generation and plastic material flow, which results in severe influence on the TMAZ size [33]. In addition, it is found that when the pin root diameter increases, the TMAZ boundaries at the top and bottom of the workpiece remain unchanged, while it is significantly enlarged at the middle part of the workpiece (i.e., from z = 1 mm to z = 5 mm) . For example, as shown in Fig. 6a, when the pin root diameter increases from 3.2 mm to 5.6 mm, the width of the TMAZ

boundary at z = 4 mm horizontal plane significantly increases from 4.46 mm to 6.45 mm.

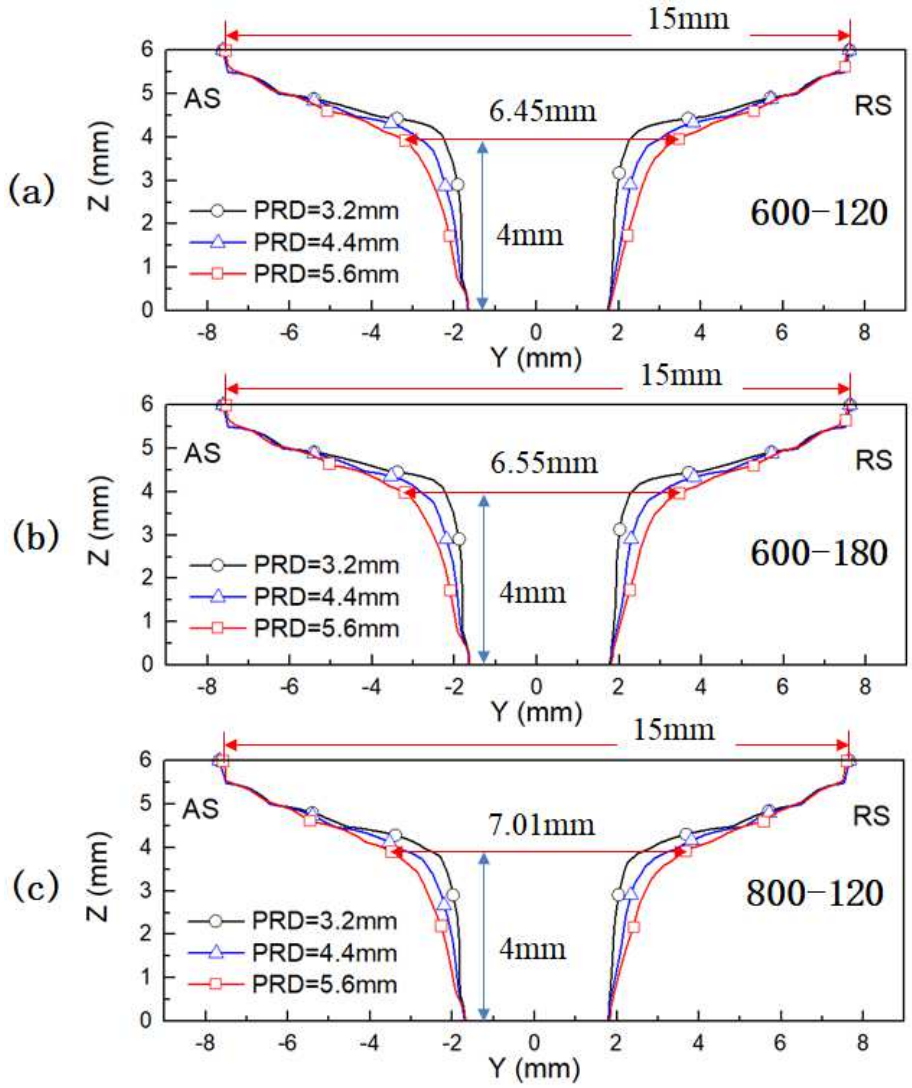

Fig. 6. Comparison of TMAZ boundaries for different pin root diameters at different welding parameters.

Fig. 7 shows the calculated peak temperature for different PRD under three different welding parameters. As depicts from Fig. 7, the peak temperature is slightly decreased with an increase of welding speed, while it is significantly increased with an increase of rotation speed. That is attributed to the fact that an increase in rotational speed implies more heat generation and results in higher peak temperature, while a higher welding speed could lead to more severe heat dissipation and results in slightly lower peak temperature [34]. In addition, by comparing the calculated peak

temperature at different pin root diameters, it is demonstrated that the peak temperature is increased with an increase of pin root diameter. This is mainly because tangential velocity at pin root and workpiece contact interface is increased when the pin root diameter increases. Thus, the heat flux at the interface increases according to Eq.(8). In addition, the contact areas between the pin and the workpiece are increased as the pin root diameter increases, which also results in more heat generation and higher peak temperature.

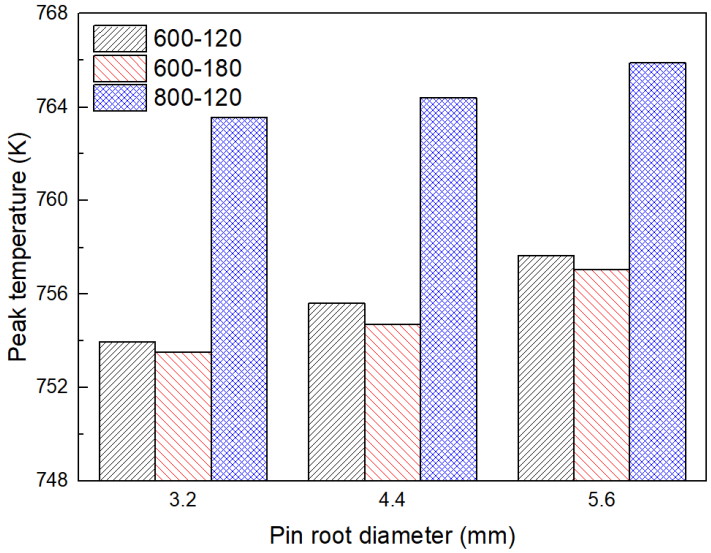

Fig. 7. Comparison of peak temperature for different pin root diameters at different welding parameters.

Fig. 8 shows temperature fields at transverse cross-section for different pin root diameters. It can be seen the temperature of the advancing side (AS) is higher than that of the retreating side (RS). It is found that although the pin root diameter is different, there is little change in the range of high-temperature region (temperature above 650 K). However, with the increase of the pin root diameter, the range of temperature over 750 K increased slightly. It illustrates that the pin root diameter has little influence on the thermal field in FSW. This is because the heat generated from the tool pin is relatively less compared with that from tool shoulder.

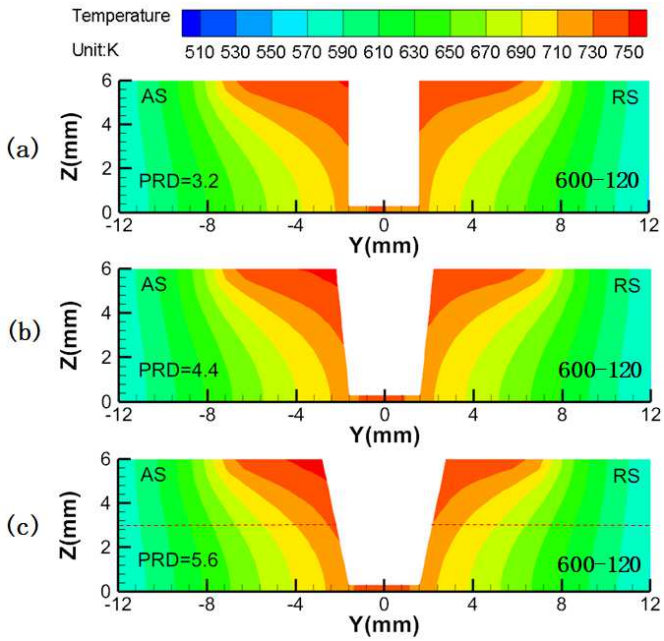

Fig. 8. Comparison of temperature fields at transverse cross-section for different pin root diameters.

Fig. 9a and Fig. 9b shows the temperature along y-axis (as shown in Fig. 8c marked with red curve) and x-axis (i.e. along the joint line) at z = 3 mm horizontal plane for different pin root diameters, respectively. Fig. 9a depicts that the temperature of the material near the tool axis (i.e., y ranges from -8 mm to 7 mm) is increased as the pin root diameter increases. Fig. 9b illustrates that the temperature of the workpiece material near the tool axis (i.e., x ranges from -8 mm to 6 mm) is increased with an increase of the pin root diameter. Outside the above regions, the temperature keeps almost the same for different pin root diameters.

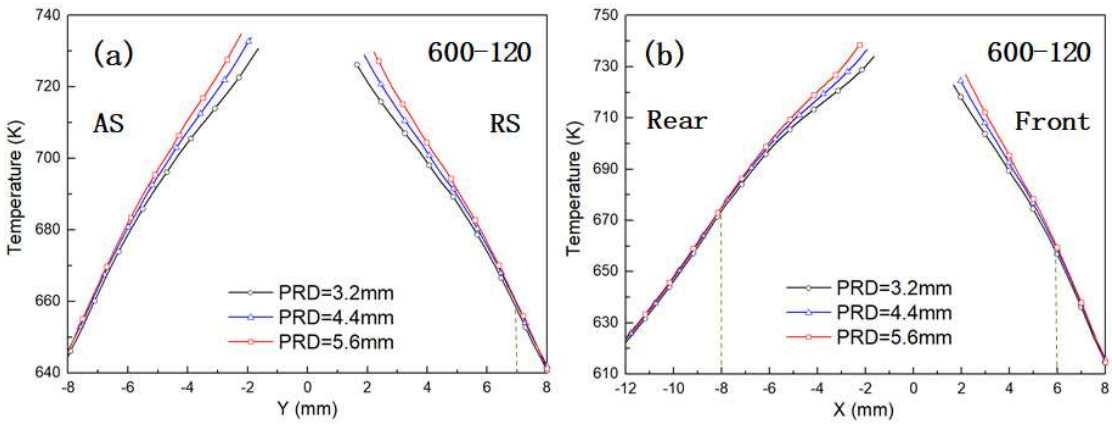

Fig. 9. Comparisons of temperature along (a) y-axis and (b) x-axis at z = 3 mm horizontal plane

Fig. 10 shows the velocity contours and vectors at z = 3 mm horizontal plane for different pin root diameters. The basic plastic material flow behavior has not changed obviously for different pin root diameters. Driven by the rotation of the tool, the material in front of the tool flows through the retreating side and flows out from the rear of the tool. However, when the pin root diameters are 3.2 mm, 4.4 mm and 5.6 mm, the corresponding maximum velocities are 0.046 m/s, 0.059 m/s, and 0.071 m/s at z = 3mm horizontal plane, respectively. That indicates the flow velocity of the materials is increased with an increase of the pin root diameter. It could be explained by Eq.(5) which indicates that the velocity of the pin-workpiece interface is increased with an increase of radial distance. In addition, the flow region is enlarged and the material flow velocity is higher at the same location for a larger pin root diameter as shown in Fig. 10, which implies that the pin root diameter significantly affects the material flow behavior near the tool although it has a slight influence on the temperature field near the tool.

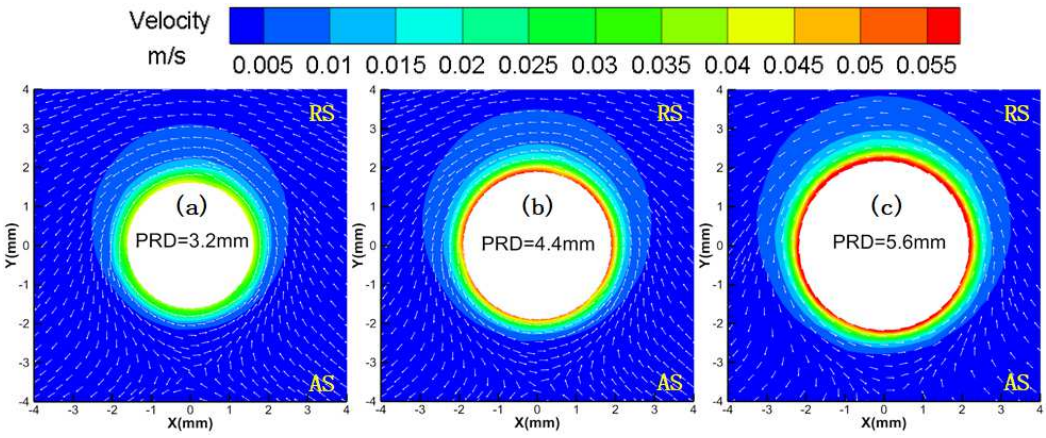

Fig. 10. Comparisons of velocity contours and vectors at z = 3mm horizontal plane for different pin root diameters.

Fig. 11 compares the temperature, viscosity and material flow velocity near the tool along z = 3.0 mm and r = 2.4 mm circular curve (as shown in Fig. 11a) for different pin root diameter. Fig. 11b illustrates that the temperature is increased with an increase of the pin root diameter. Meanwhile, the highest temperature of the material around the tool appeared in the rear of the AS for different PRD. Fig. 11c shows that the viscosity is decreased with the increase of the pin root diameter. This is

mainly because more heat is generated from the tool pin as the pin root diameter increases. Furthermore, the radial distance from the pin side surface to the monitoring curve is decreased, which results in more severe softening effect for a larger PRD. Fig. 11d depicts that the flow velocity of materials is higher for a larger PRD. This is due to more heat generation and higher temperature with lower viscosity for a larger PRD which results in a higher material flow velocity near the tool. In addition, the flow velocity at the AS is lower than that at the RS for different pin root diameters. This is mainly because the viscosity of the material on the AS is higher and the fluidity of the material is worse.

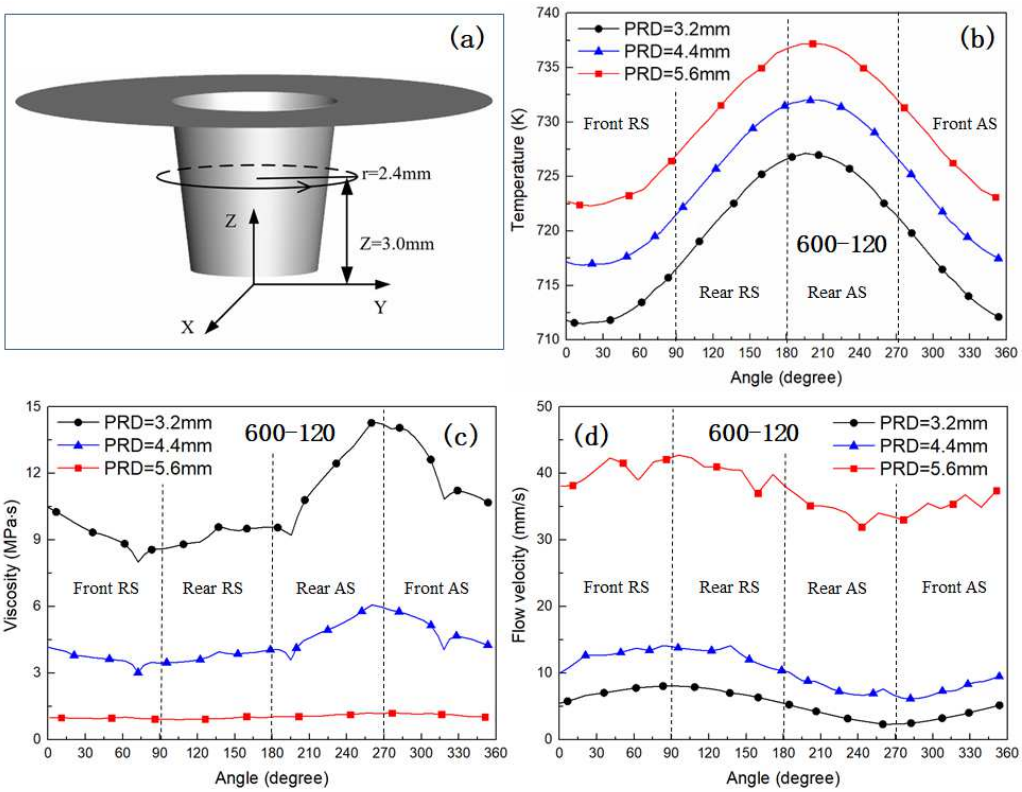

Fig. 11. (a) Schematic drawing of the location at z = 3.0 mm and r = 2.4 mm. Variation curves of the (b) temperature, (c) viscosity, and (d) flow velocity for different pin root diameters at the location.

4.3 The effects of pin tip diameter

In this section, the effect of the pin tip diameter on the welding thermal process and material flow in FSW is studied. The pin root diameter is 5.6 mm and remains unchanged. Fig. 12a shows the predicted total tool torque, pin torque and its fraction for different pin tip diameters. It depicts that the total tool torque remains almost the

same for three different pin tip diameters considered in this paper. However, the pin torque and its fraction are significantly increased when a larger pin tip diameter is employed for welding. This is also because the increase of the pin tip diameter makes the contact areas between the pin and the workpiece increase. Fig. 12b illustrates that the total transverse force is slightly decreased when using a larger pin tip diameter. However, the transverse force imposed on the tool pin is significantly increased and its fraction reaches almost 45% of the total transverse force when the pin diameter is increased to 5.6 mm. It implies that transverse force imposed on a tapered cylindrical pin is lower than on a cylindrical pin.

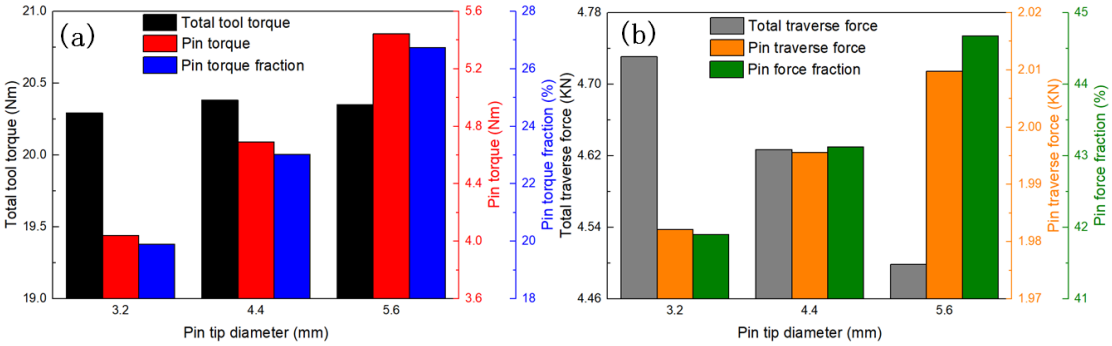

Fig. 12. Comparison of (a) torque and (b) transverse force for different pin tip diameters.

Fig. 13 shows the predicted TMAZ boundaries for different pin tip diameters. The maximum width at the top of TMAZ boundary is not affected by the pin tip diameter. In the region of z < 5mm, the closer to the bottom of the workpiece, the greater the TMAZ boundary changes with the pin tip diameter. When the pin tip diameters are 3.2 mm, 4.4 mm and 5.6 mm, the corresponding minimum width of the TMAZ boundaries at the bottom surface of the workpiece are 3.4 mm, 4.77 mm and 6.03 mm. It implies that the shear layer thicknesses for different pin tip diameters are 0.1 mm, 0.18 mm and 0.21 mm, respectively. This indicates that the larger the pin tip diameter is, the more materials at the lower part of the workpiece are subjected to the shearing action of the pin.

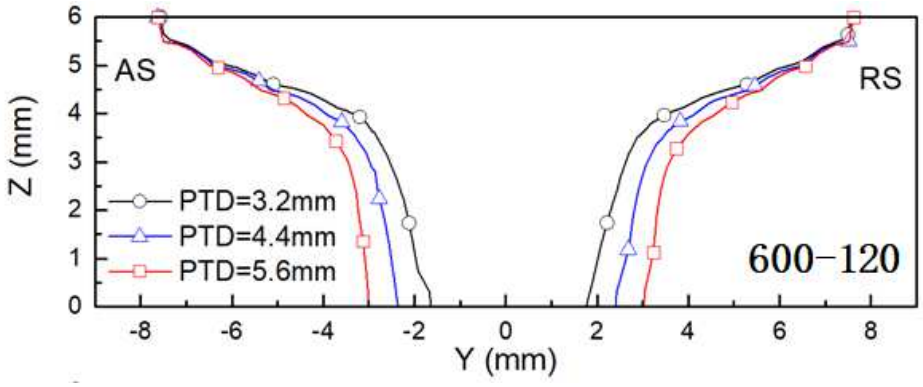

Fig. 13. Comparison of TMAZ boundaries for different pin tip diameters.

Fig. 14 shows the temperature field contours at the transverse cross-section for different pin tip diameters. When the pin tip diameters are 3.2 mm, 4.4 mm and 5.6 mm, the corresponding peak temperatures are 758 K, 760 K and 767 K, respectively. This indicates that the pin tip diameter slightly influence the peak temperature of the workpiece. In addition, it is found that the range of high temperature (temperature above 650 K) expands with an increase of the pin tip diameter, especially the temperature fields at the middle and lower part of workpiece.

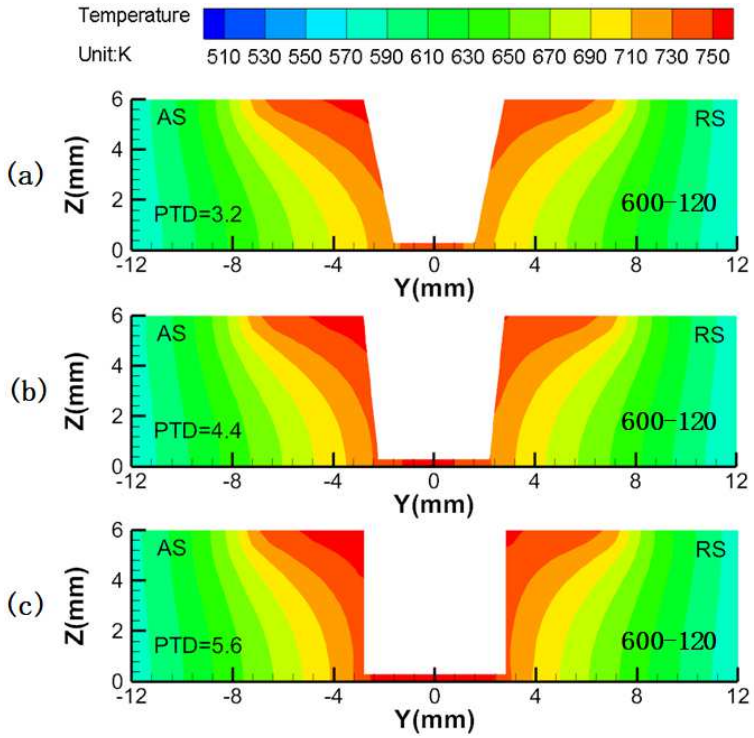

Fig. 14. Comparison of temperature fields at transverse cross-section for different pin tip diameters.

Fig. 15 shows the velocity contours and vectors at z = 3 mm horizontal plane for different pin tip diameters. When the pin tip diameters are 3.2 mm, 4.4 mm and 5.6 mm, the corresponding maximum velocities are 0.071 m/s, 0.081 m/s, and 0.091 m/s at z = 3 mm horizontal plane, respectively. In addition, it could be seen that more plastic material near the tool could rotate around the tool with an increase of the pin tip diameter.

Fig. 16 compares the temperature, viscosity and material flow velocity near the tool along z = 3.0 mm and r = 2.4 mm circular curve (as shown in Fig. 16a) for different pin tip diameters. Fig. 16b and Fig. 16c depict that at the same radial distance, the larger the pin tip diameter is, the higher the temperature is, and the lower the viscosity is. This is mainly because the radial distance between the monitored curves and the pin side surface is smaller at the condition with a larger pin tip diameter. Thus, the severe heat generation and plastic deformation with larger pin tip diameter will lead to higher temperature with smaller viscosity due to more severe thermal softening. At the same time, the difference between viscosity at AS and at RS is more severe at a smaller pin tip diameter as shown in Fig. 16c. Fig. 16d shows that the velocity at the same radial distance is increased with an increase of the pin tip diameter. This is mainly because the viscosity for the case with a larger pin tip diameter is lower and its fluidity is better, which results in higher material flow velocity.

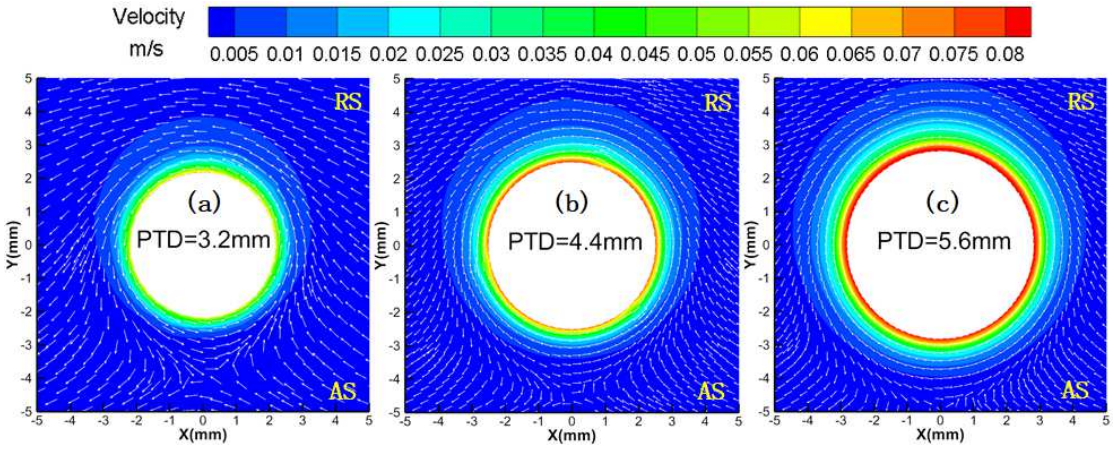

Fig. 15. Comparisons of velocity contours and vectors at z = 3mm horizontal plane for different pin tip diameters.

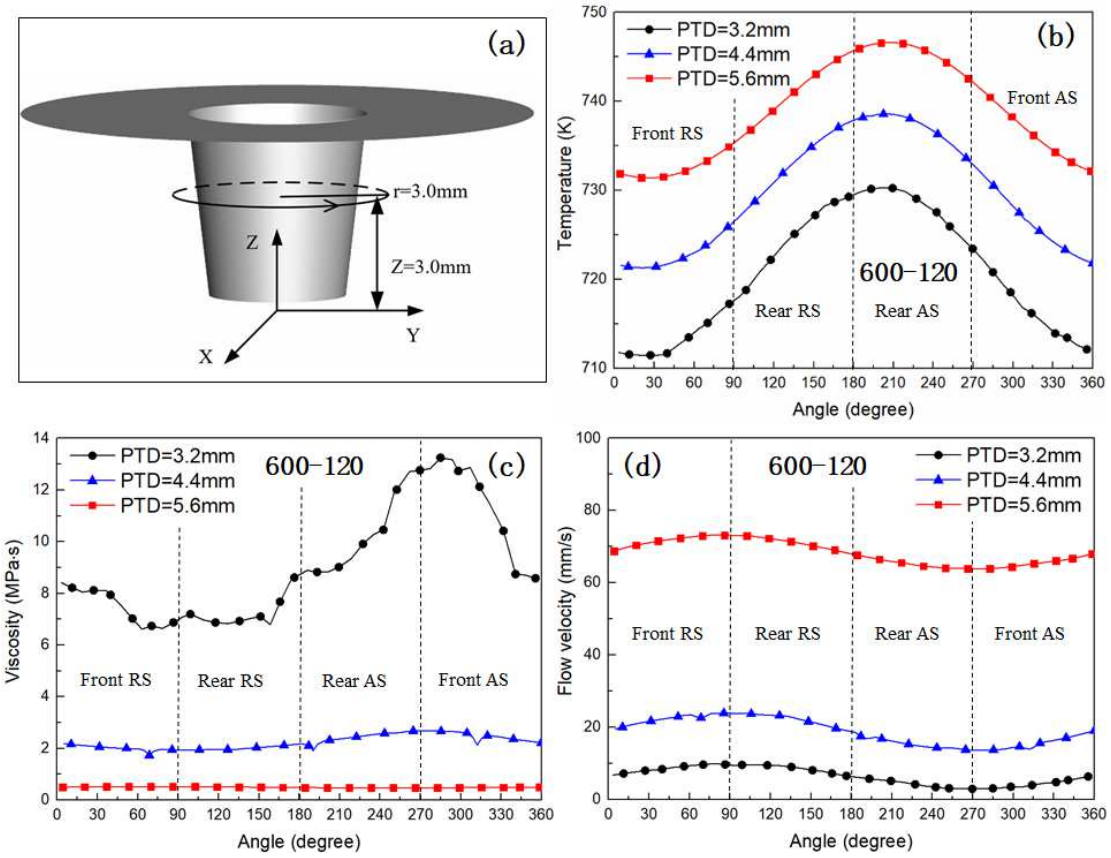

Fig. 16. (a) Schematic drawing of the location at z = 3 mm and r = 3 mm. Variation curves of the (b) temperature, (c) viscosity, and (d) flow velocity for different pin tip diameters at the location.

4.4 The effects of pin size in condition of certain taper angle

In this section, the effects of pin size for the same shape on the FSW thermal process and material flow were quantitatively studied, by simultaneously changing the pin root diameter and pin tip diameter and keeping its taper angle $\Phi = 12°$ without changing its tapered cylindrical shape. Fig. 17a shows the calculated total tool torque, pin torque and its fraction for different pin sizes, while Fig. 17b correspondingly illustrates transverse force. Fig. 17a depicts that the total tool torque vary a little under different pin sizes at the same taper angle, while the pin torque and its fraction are significantly increased with a larger pin. For example, as the pin root diameter increases from 5.0 mm to 6.2 mm (with its PTD correspondingly increases from 2.6 mm to 3.8 mm), the pin tool torque is increased from 3.3 Nm to 4.8 Nm, and its fraction is increased from 16% to 24%. Fig. 17b illustrates that the transverse force shows similar trends as the pin torque. They imply that the larger the pin is, the higher

torque and transverse force imposed on the pin.

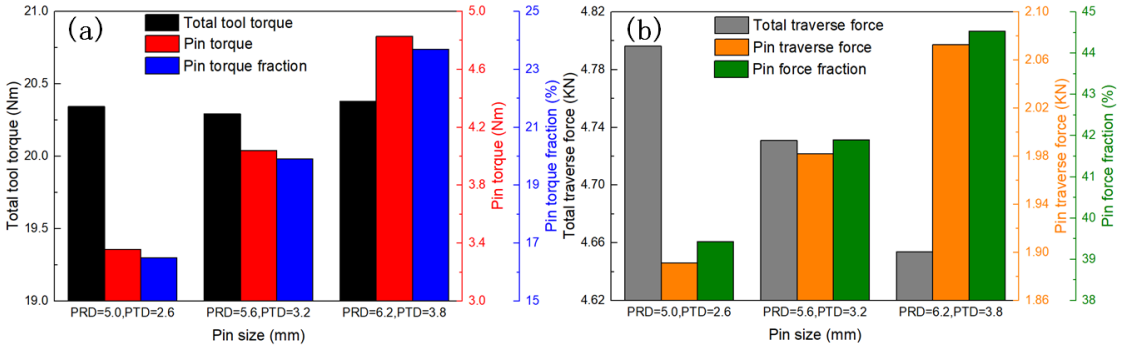

Fig. 17. Comparison of (a) torque and (b) transverse force for different pin sizes.

Fig. 18 shows the TMAZ boundaries for different pin sizes when the tool rotation speed is 600 rpm and welding speed is 120 mm/min. As is seen, the maximum width at the top of the TMAZ boundary is not affected by the size of the pin. In the range from z = 4 mm to z = 5 mm, the closer the location is to the top of the workpiece, the less the TMAZ boundary changes with the pin size. However, in the region of $z < 4$ mm, the variation of TMAZ boundary with the pin size is almost the same at different heights.

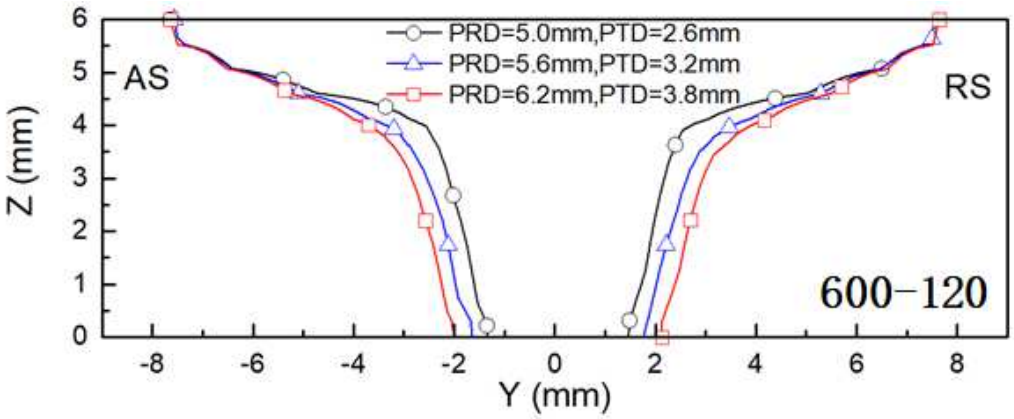

Fig. 18. Comparison of TMAZ boundaries for different pin sizes.

Fig. 19 compares the temperature, viscosity and material flow velocity near the tool along z = 3.0 mm and r = 2.4 mm circular curve (as shown in Fig. 19a) for different sizes. It can be seen from Fig. 19 that the temperature near the tool is increased with an increase of the tool pin size, while the viscosity is reduced when a larger tool pin is employed. In addition, Fig. 19c depicts that the amplitude of

viscosity variation is reduced when the tool pin size is increased. Fig. 19d shows that the material flow velocity at the same radial distance near the tool is higher when using a larger tool pin size. This is due to more severe thermal softening with a larger pin which would generate more heat. Thus, the viscosity of the material is lower and its fluidity is better.

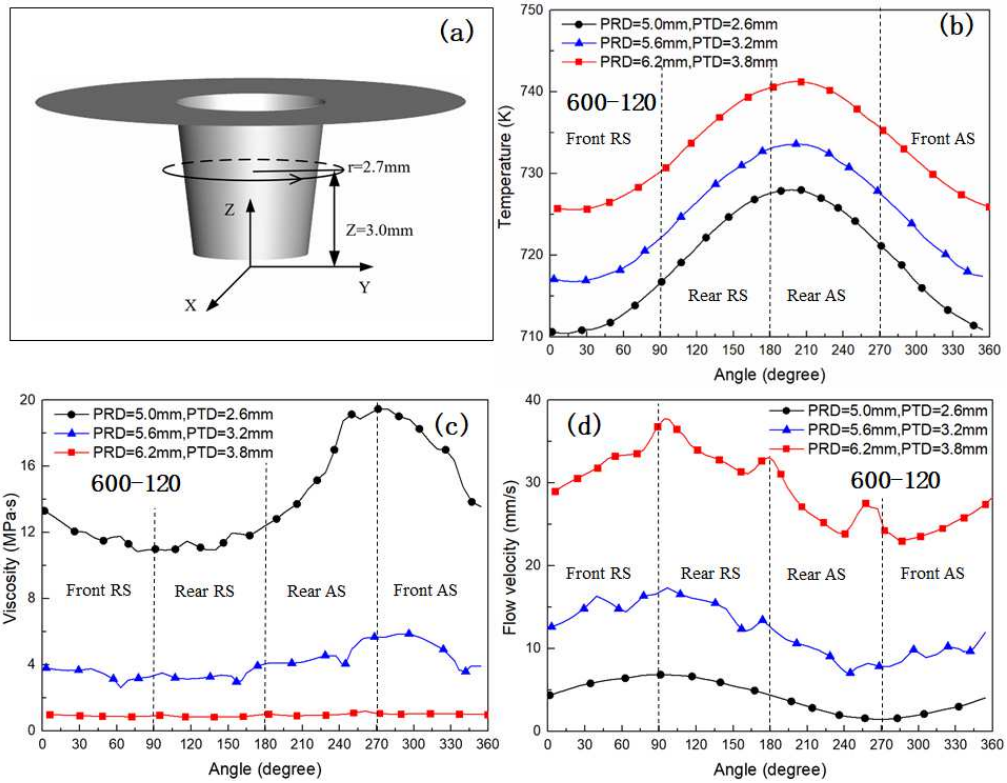

Fig. 19. (a) Schematic drawing of the location at z = 3 mm and r = 2.7 mm. Variation curves of the (b) temperature, (c) viscosity, and (d) flow velocity for different pin size at the location.

5. Conclusions

(1) An integrated CFD model was adopted to quantitatively analyze the effect of pin size and taper angle on the thermal process and plastic material flow behaviors in FSW process. The predicted thermal cycles and TMAZ boundaries agree with the experimental measured ones.

(2) The torque and transverse force imposed on the pin are significantly increased with an increase of the pin root diameter. The temperature and material flow velocity near the tool at the same radial distance are increased with a larger pin root diameter. When the pin root diameter increases, the minimum width of TMAZ boundary in the bottom surface of the workpiece and the maximum width in the top

surface remain unchanged, while the width of TMAZ in the middle of the workpiece is increased sharply.

(3) Similarly, the torque and transverse force imposed on the pin are increased with the increase of the pin tip diameter. However, the viscosity near the pin is decreased, which results in better fluidity of plastic material and higher flow velocity. The shear layer thickness of the same horizontal plane in the region of $z < 5$ mm is increased when using a pin with larger tip diameter, while the maximum width of the TMAZ at the top surface is not affected by the pin tip diameter.

(4) It reveals that the pin size and taper angle have little effect on the thermal field. However, it indeed significantly affect the plastic material flow behaviors such as expanding the shear zone, increasing the material flow region and velocity. The pin size and taper angle slightly affect the total tool torque and transverse force. However, they significantly determine the torque and transverse force imposed on the pin, which would final determine the service life of the tool.

Author contribution

Jie Chen: Conceptualization, Formal analysis, Investigation, Writing - original draft. **Lei Shi**: Methodology, Supervision, Project administration, Funding acquisition, Writing - review and editing. **Chuansong Wu:** Funding acquisition, Project administration, Validation. **Yuanning Jiang:** Investigation; Validation.

Declarations

Ethics approval and consent to participate No applicable.
Consent for publication Authors consent to publish this article.
Competing interests The authors declare no competing interests.

Acknowledgements

This work is supported by the National Natural Science Foundation of China (Grant No. 51905309 and 52035005) and Qilu Young Scholar Program of Shandong University.

References

[1] He X, Gu F, Ball A. A review of numerical analysis of friction stir welding. Prog Mater Sci 2014;65:1-66.

[2] Threadgill PL, Leonard AJ, Shercliff HR, Withers PJ. Friction stir welding of aluminium alloys. Int Mater Rev 2009;54(2):49-93.

[3] Chen K, Liu X, Ni J. A review of friction stir-based processes for joining dissimilar materials. Int J Adv Manuf Technol 2019;104:1709-1731.

[4] Nandan R, Debroy T, Bhadeshia H. Recent advances in friction-stir welding-process, weldment structure and properties. Prog Mater Sci 2008;53(6):980-1023.

[5] Mugada KK, Adepu K. Influence of tool shoulder end features on friction stir weld characteristics of Al-Mg-Si alloy. Int J Adv Manuf Technol 2018:88:1553-1566.

[6] Rai R, De A, Bhadeshia HKDH, DebRoy T. Review: friction stir welding tools. Sci Technol Weld Joining 2011;16(4):325-342.

[7] Mirzaei M, Asadi P, Fazli A. Effect of tool pin profile on material flow in double shoulder friction stir welding of AZ91 magnesium alloy. Int J Mech Sci 2020;183:105775.

[8] Suresha CN, Rajaprakash BM, Upadhya S. A study of the effect of tool pin profiles on tensile strength of welded joints produced using friction stir welding process. Mater Manuf Processes 2011;26(9):1111-1116.

[9] Quintana KJ, Silveira JLL. Mechanistic models and experimental analysis for the torque in FSW considering the tool geometry and the process velocities. J Manuf Process 2017;30:406-417.

[10] Elangovan K, Balasubramanian V. Influences of tool pin profile and tool shoulder diameter on the formation of friction stir processing zone in AA6061 aluminium alloy. Mater Design 2008;29(2):362-373.

[11] Marzbanrad J, Akbari M, Asadi P, Safaee S. Characterization of the influence of tool pin profile on microstructural and mechanical properties of friction stir welding. Metall Mater Trans B 2014;45(5):1887-1894.

[12] Prakash P, Anand RS, Jha SK. Prediction of weld zone shape with effect of tool pin profile in friction stir welding process. J Mech Sci Technol 2020;34(1):279-287.

[13] Su H, Wu CS, Bachmann M, Rethmeier M. Numerical modeling for the effect of pin profiles on thermal and material flow characteristics in friction stir welding. Mater Design 2015;77:114-125.

[14] Akbari M, Aliha M, Keshavarz S, Bonyadi A. Effect of tool parameters on mechanical properties, temperature, and force generation during FSW. Proc Inst Mech Eng, Part L 2019;233(6):1033-1043.

[15] Kulekci MK, Şik A, Kaluç E. Effects of tool rotation and pin diameter on fatigue

properties of friction stir welded lap joints. Int J Adv Manuf Technol 2008;36(9-10):877-882.

[16] Ramachandran KK, Murugan N, Shashi Kumar S. Effect of tool axis offset and geometry of tool pin profile on the characteristics of friction stir welded dissimilar joints of aluminum alloy AA5052 and HSLA steel. Mater Sci Eng A 2015;639:219-233.

[17] Zhang Z, Wu Q, Zhang H. Numerical studies of effect of tool sizes and pin shapes on friction stir welding of AA2024-T3 alloy. T Nonferr Metal Soc 2014;24(10):3293-3301.

[18] Buffa G, Hua J, Shivpuri R, Fratini L. Design of the friction stir welding tool using the continuum based FEM model. Mater Sci Eng A 2006;419(1-2):381-388.

[19] Nandan R, Roy GG, Lienert TJ, DebRoy T. Numerical modelling of 3D plastic flow and heat transfer during friction stir welding of stainless steel. Sci Technol Weld Joining 2006;11(5):526-537.

[20] Chen G, Shi Q, Li Y, Sun Y, Dai Q, Jia J, et al. Computational fluid dynamics studies on heat generation during friction stir welding of aluminum alloy. Comp Mater Sci 2013;79:540-546.

[21] Shi L, Wu CS, Liu HJ. The effect of the welding parameters and tool size on the thermal process and tool torque in reverse dual-rotation friction stir welding. Int J Mach Tools Manuf 2015;91:1-11.

[22] Colegrove PA, Shercliff HR. 3-Dimensional CFD modelling of flow round a threaded friction stir welding tool profile. J Mater Process Technol 2005;169(2):320-327.

[23] Sheppard T, Jackson A. Constitutive equations for use in prediction of flow stress during extrusion of aluminium alloys. Mater Sci Technol 1997;13(3):203-209.

[24] Arora A, De A, DebRoy T. Toward optimum friction stir welding tool shoulder diameter. Scripta Mater 2011;64(1):9-12.

[25] Schmidt H, Hattel J, Wert J. An analytical model for the heat generation in friction stir welding. Modell Simul Mater Sci Eng 2004;12(1):143-157.

[26] Chen G, Zhang S, Zhu Y, Yang C, Shi Q. Thermo-mechanical analysis of friction stir welding: A review on recent advances. Acta Metall Sin 2020;33(1):3-12.

[27] Mehta M, Chatterjee K, De A. Monitoring torque and traverse force in friction

stir welding from input electrical signatures of driving motors. Sci Technol Weld Joining 2013;18(3):191-197. 4

[28] Arora A, Mehta M, De A, DebRoy T. Load bearing capacity of tool pin during friction stir welding. Int J Adv Manuf Technol 2012;61(9-12):911-920.

[29] Ulysse P. Three-dimensional modeling of the friction stir-welding process. Int J Mach Tool Manu 2002;42(14):1549-1557.

[30] Bastier A, Maitournam MH, Dang Van K, Roger F. Steady state thermomechanical modelling of friction stir welding. Sci Technol Weld Joining 2006;11(3):278-288.

[31] Shi L, Wu CS, Fu L. Effects of tool shoulder size on the thermal process and material flow behaviors in ultrasonic vibration enhanced friction stir welding. J Manuf Process 2020;53:69-83.

[32] Su H, Wu C. Determination of the traverse force in friction stir welding with different tool pin profiles. Sci Technol Weld Joining 2019;24(3):209-217.

[33] Zeng XH, Xue P, Wang D, Ni DR, Xiao BL, Ma ZY. Effect of processing parameters on plastic flow and defect formation in friction-stir-welded aluminum alloy. Metall Mater Trans A 2018;49(7):2673-2683.

[34] Carlone P, Palazzo GS. Influence of process parameters on microstructure and mechanical properties in AA2024-T3 friction stir welding. Metallogr Microstruct Anal 2013;2(4):213-222.

Figure captions:

Fig. 1. Schematic drawing of the friction stir welding (FSW) process.

Fig. 2. Schematic drawing of the tool geometry.

Fig. 3. Calculated and measured thermal cycles at the point (a) 10 mm and (b) 20 mm away from the weld centerline.

Fig. 4. Calculated and measured TMAZ boundary in weld cross-section.

Fig. 5. Comparison of (a) torque and (b) transverse force for different pin root diameters.

Fig. 6. Comparison of TMAZ boundaries for different pin root diameters at different welding parameters.

Fig. 7. Comparison of peak temperature for different pin root diameters at different welding parameters.

Fig. 8. Comparison of temperature fields at transverse cross-section for different pin root diameters.

Fig. 9. Comparisons of temperature along (a) *y-axis* and (b) *x-axis* at z = 3 mm horizontal plane

Fig. 10. Comparisons of velocity contours and vectors at z = 3mm horizontal plane for different pin root diameters.

Fig. 11. (a) Schematic drawing of the location at z = 3.0 mm and r = 2.4 mm. Variation curves of the (b) temperature, (c) viscosity, and (d) flow velocity for different pin root diameters at the location.

Fig. 12. Comparison of (a) torque and (b) transverse force for different pin tip diameters.

Fig. 13. Comparison of TMAZ boundaries for different pin tip diameters.

Fig. 14. Comparison of temperature fields at transverse cross-section for different pin tip diameters.

Fig. 15. Comparisons of velocity contours and vectors at z = 3mm horizontal plane for different pin tip diameters.

Fig. 16. (a) Schematic drawing of the location at z = 3 mm and r = 3 mm. Variation curves of the (b) temperature, (c) viscosity, and (d) flow velocity for different pin tip diameters at the location.

Fig. 17. Comparison of (a) torque and (b) transverse force for different pin sizes.

Fig. 18. Comparison of TMAZ boundaries for different pin sizes.

Fig. 19. (a) Schematic drawing of the location at z = 3 mm and r = 2.7 mm. Variation curves of the (b) temperature, (c) viscosity, and (d) flow velocity for different pin size at the location.

Table captions:

Table 1 Chemical compositions of 2024-T3 aluminum alloy.

Figures

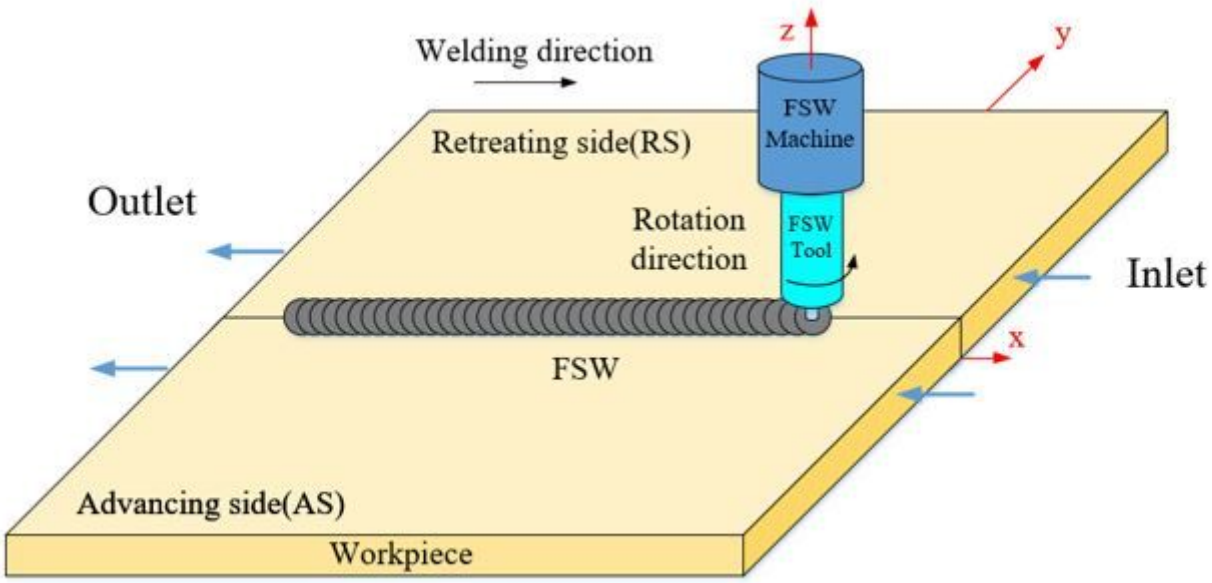

Figure 1

Schematic drawing of the friction stir welding (FSW) process.

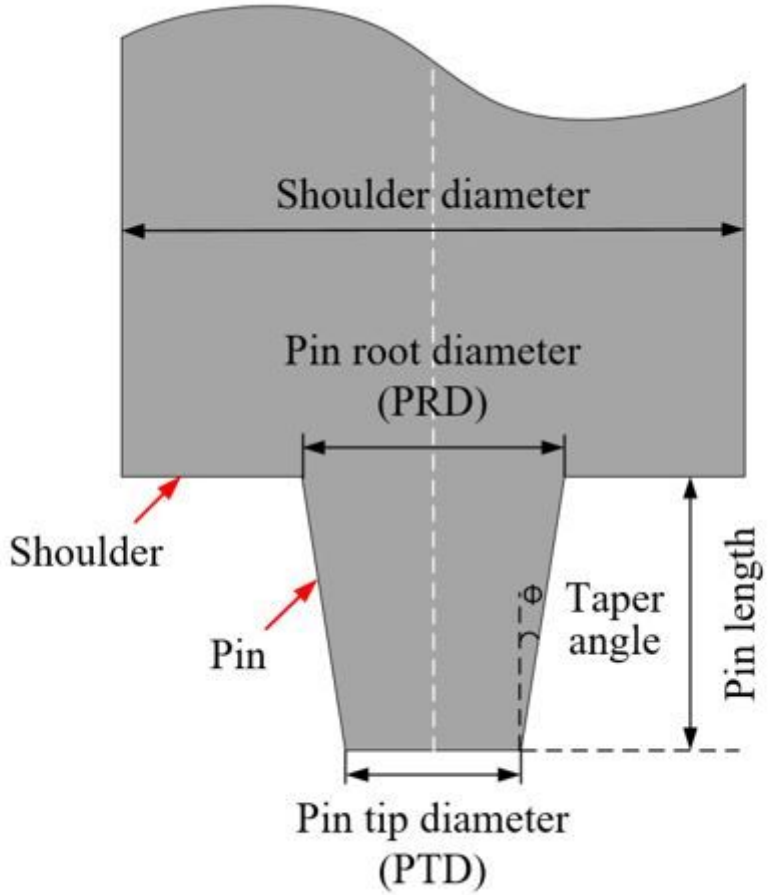

Figure 2

Schematic drawing of the tool geometry.

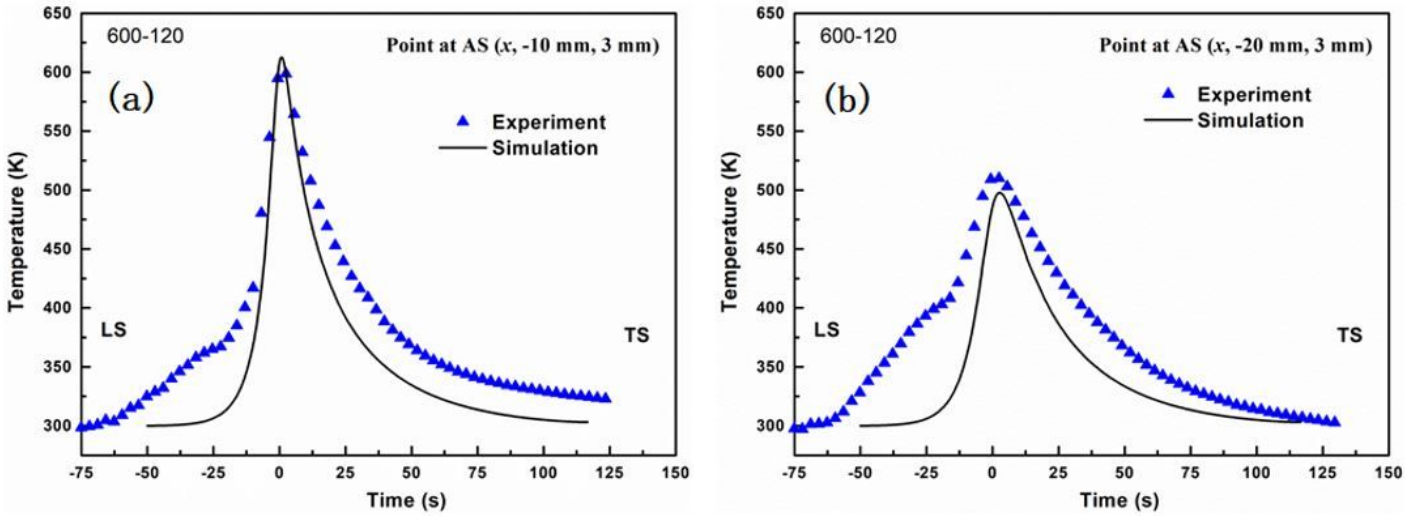

Figure 3

Calculated and measured thermal cycles at the point (a) 10 mm and (b) 20 mm away from the weld centerline.

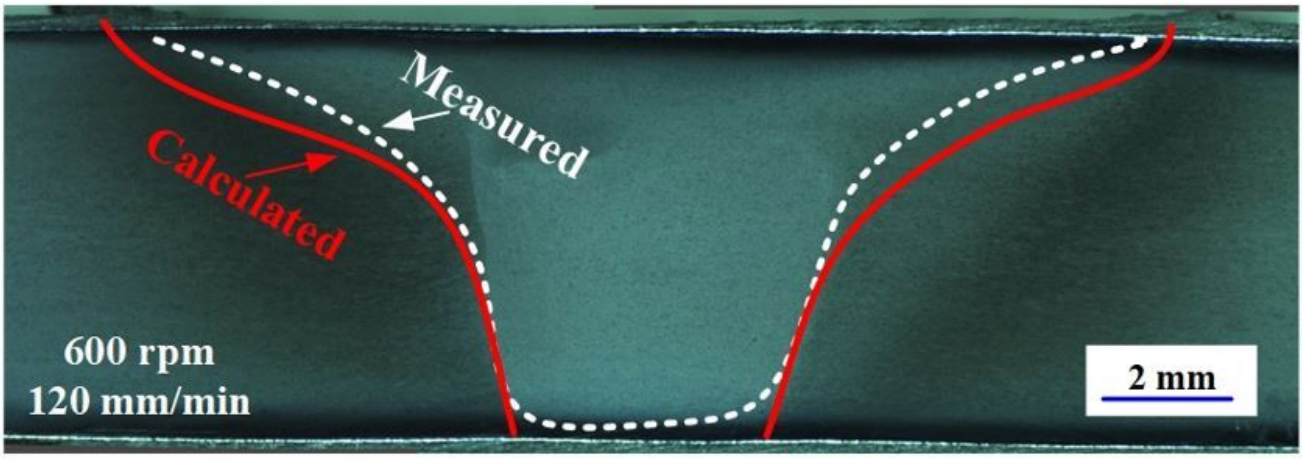

Figure 4

Calculated and measured TMAZ boundary in weld cross-section.

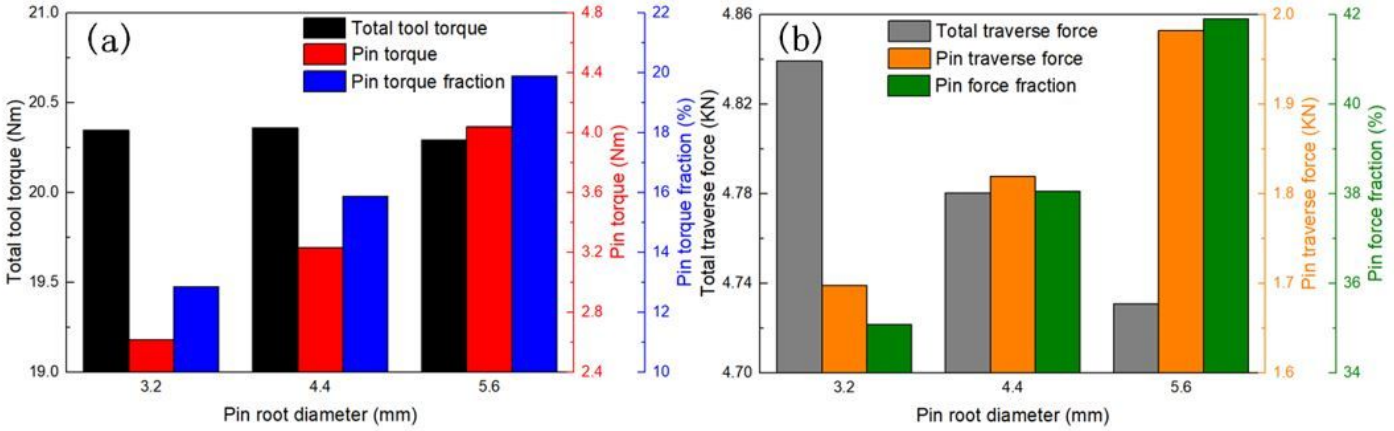

Figure 5

Comparison of (a) torque and (b) transverse force for different pin root diameters.

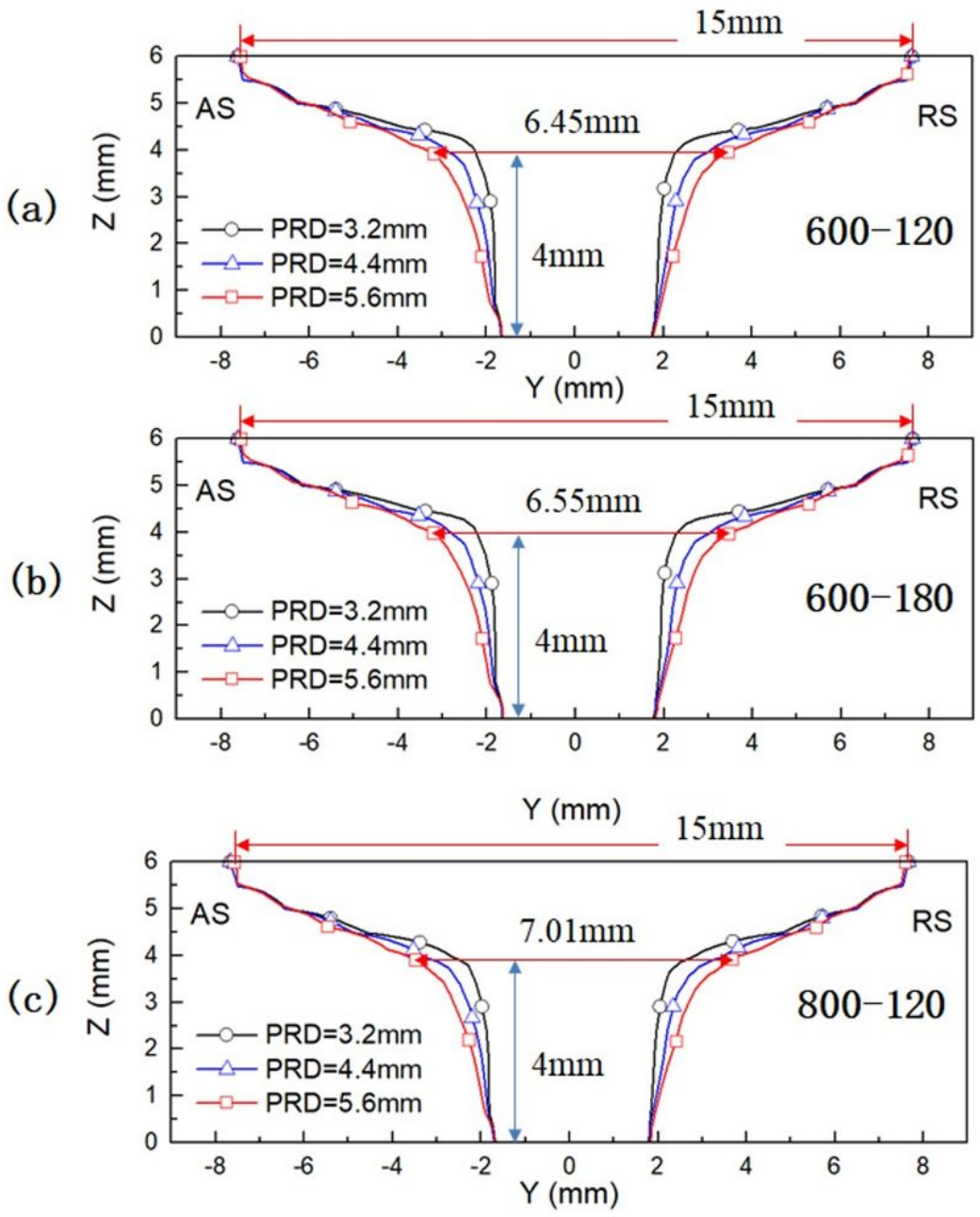

Figure 6

Comparison of TMAZ boundaries for different pin root diameters at different welding parameters.

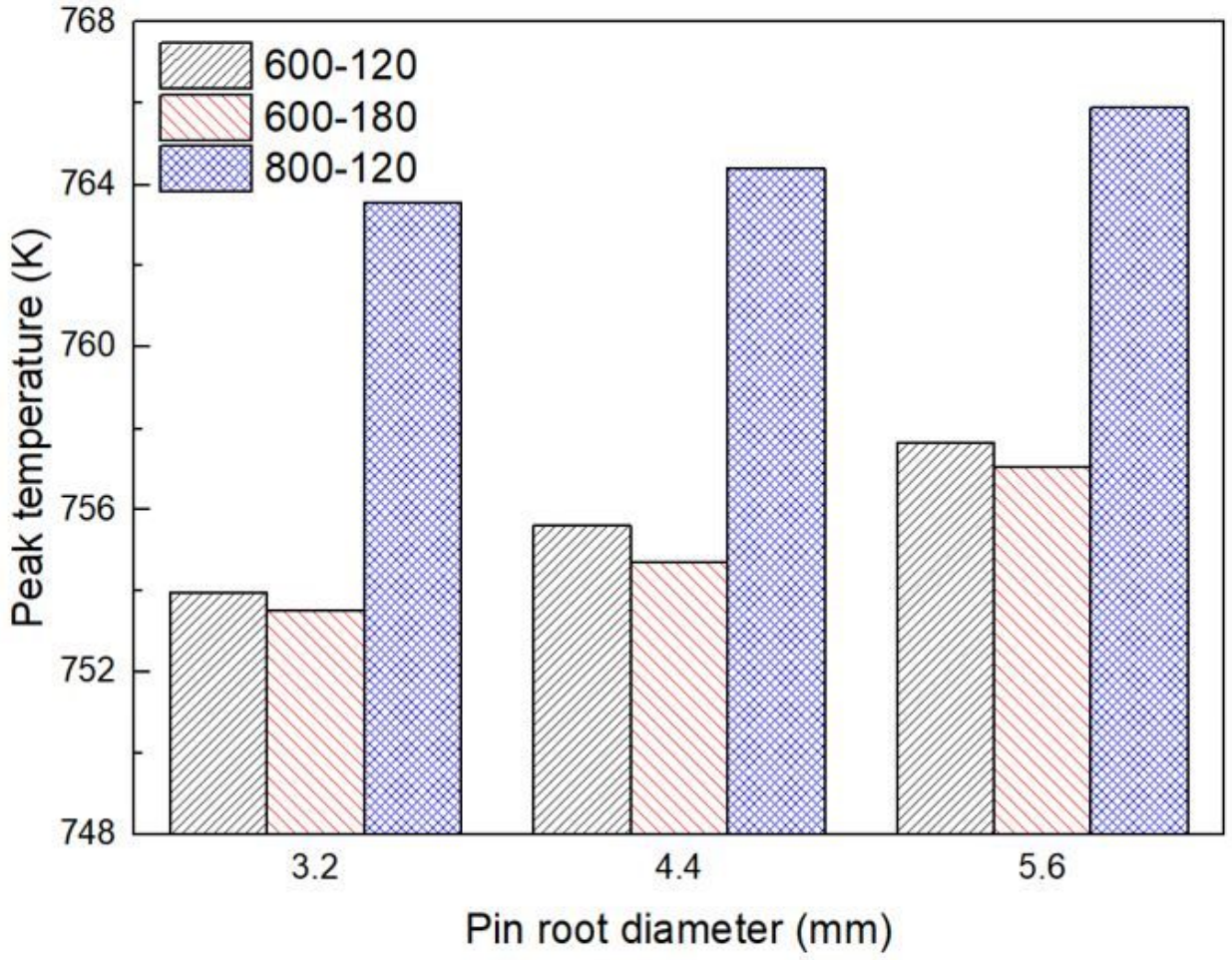

Figure 7

Comparison of peak temperature for different pin root diameters at different welding parameters.

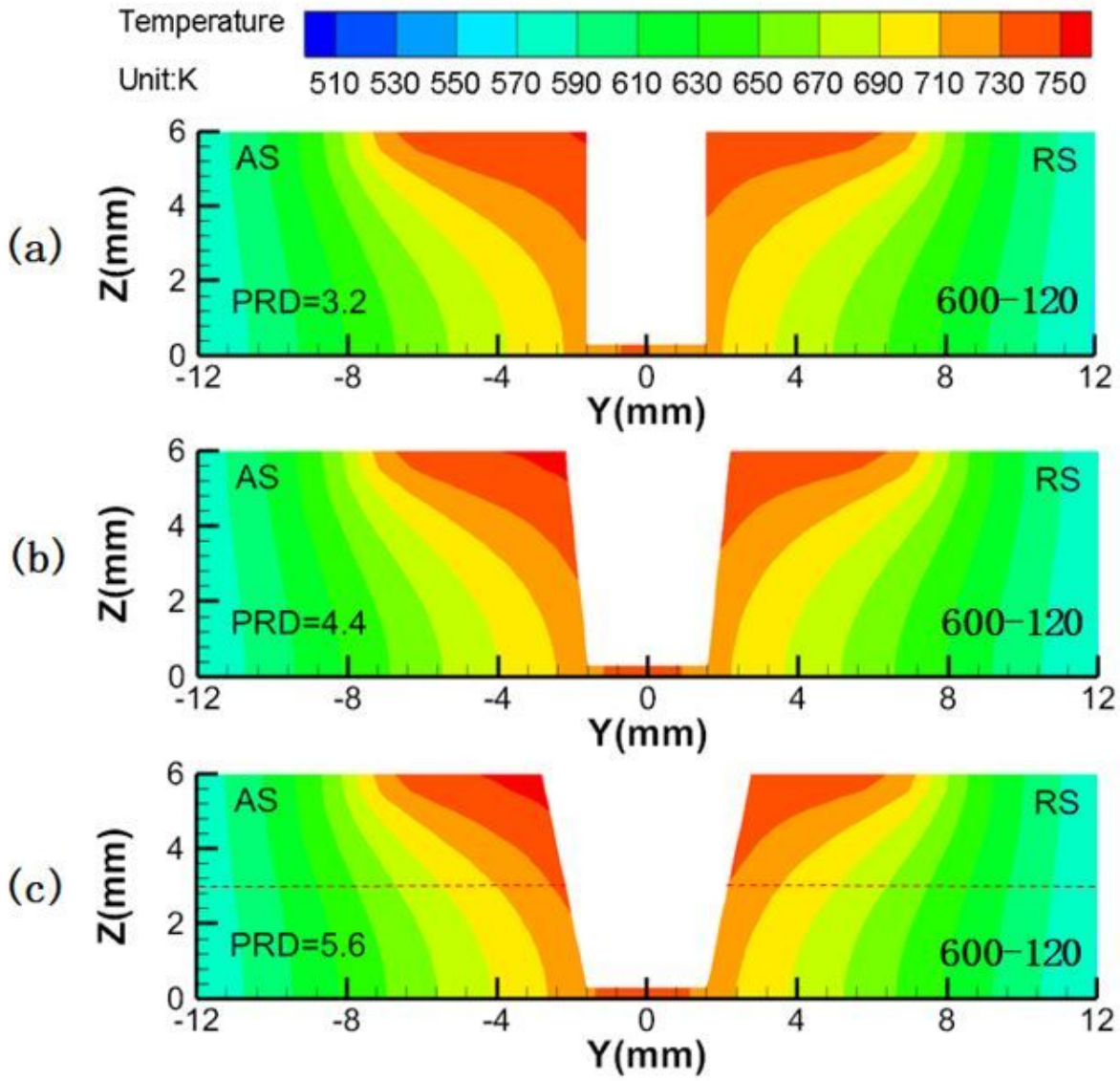

Figure 8

Comparison of temperature fields at transverse cross-section for different pin root diameters.

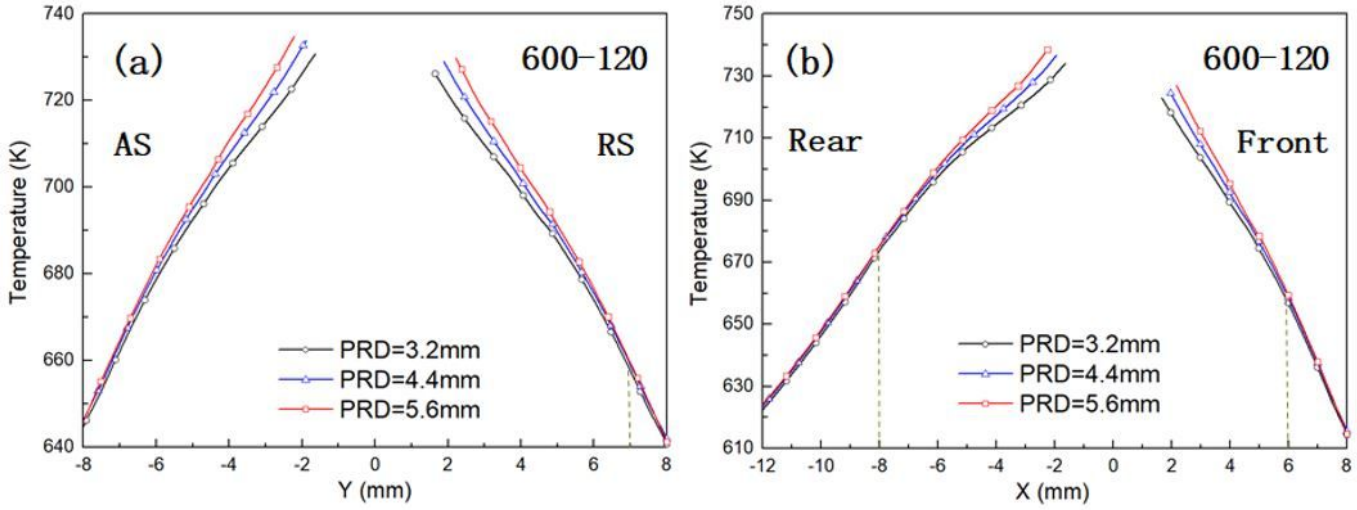

Figure 9

Comparisons of temperature along (a) y-axis and (b) x-axis at z = 3 mm horizontal plane

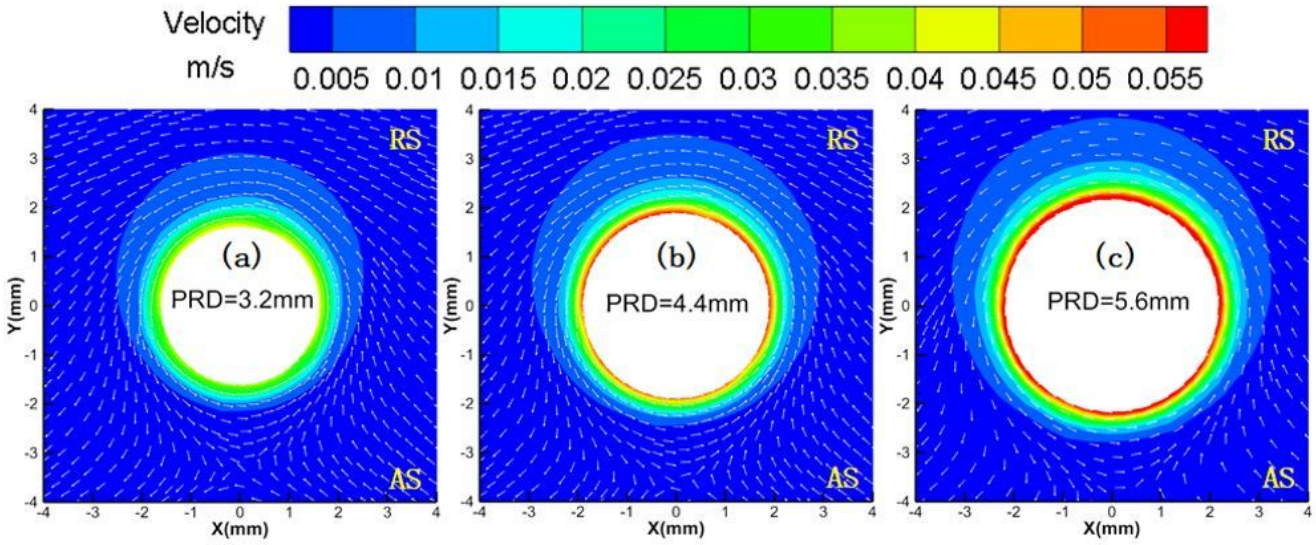

Figure 10

Comparisons of velocity contours and vectors at z = 3mm horizontal plane for different pin root diameters.

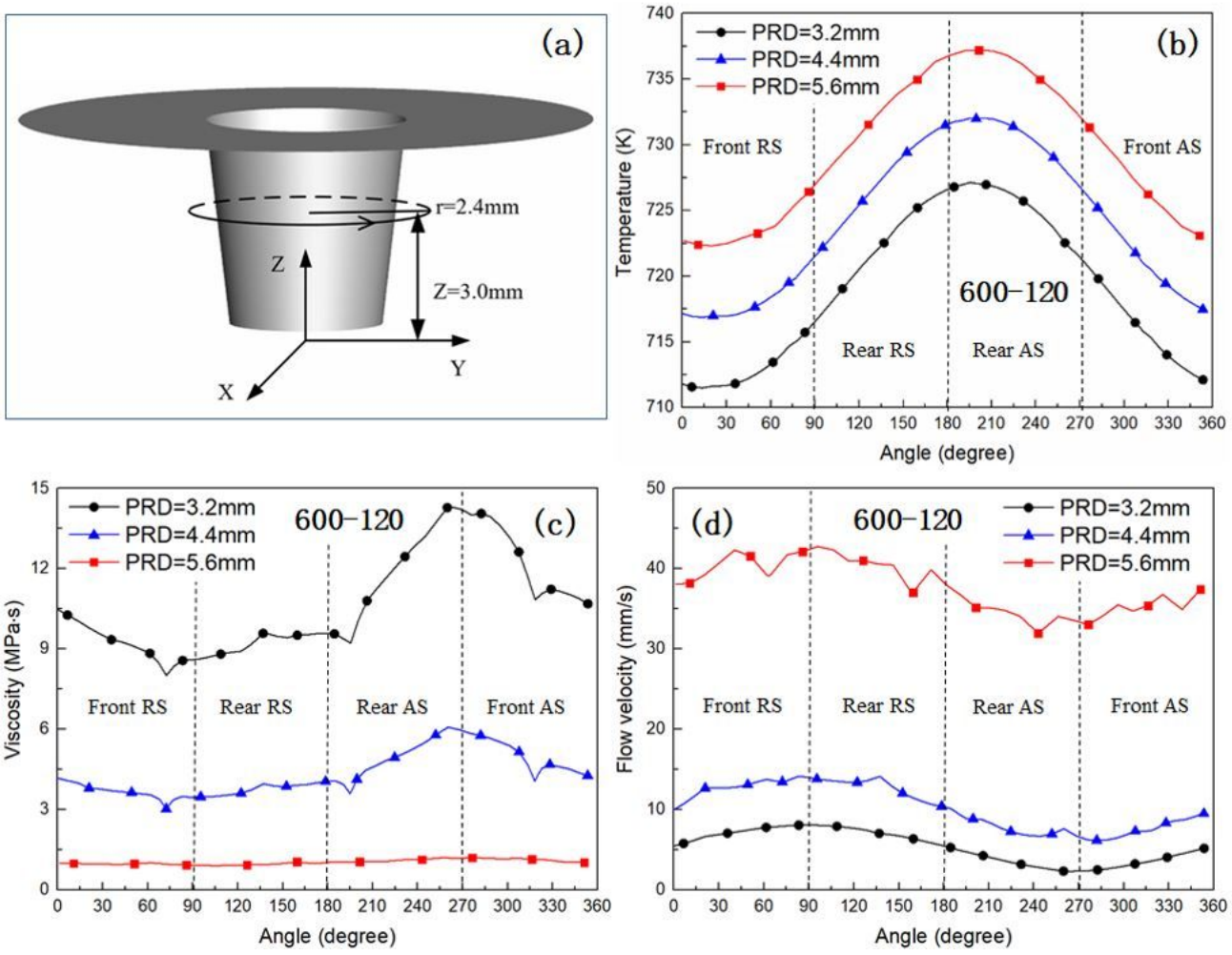

Figure 11

(a) Schematic drawing of the location at z = 3.0 mm and r = 2.4 mm. Variation curves of the (b) temperature, (c) viscosity, and (d) flow velocity for different pin root diameters at the location.

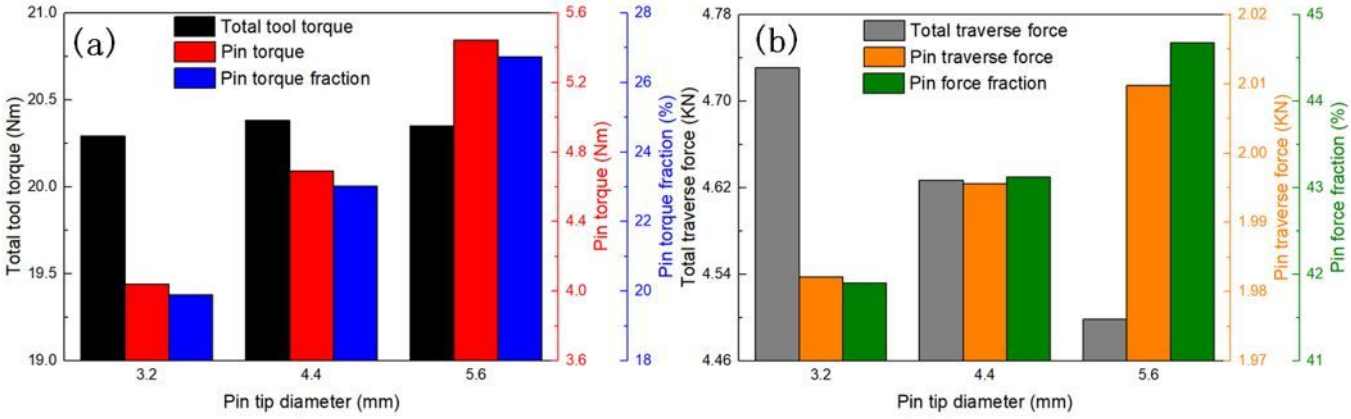

Figure 12

Comparison of (a) torque and (b) transverse force for different pin tip diameters.

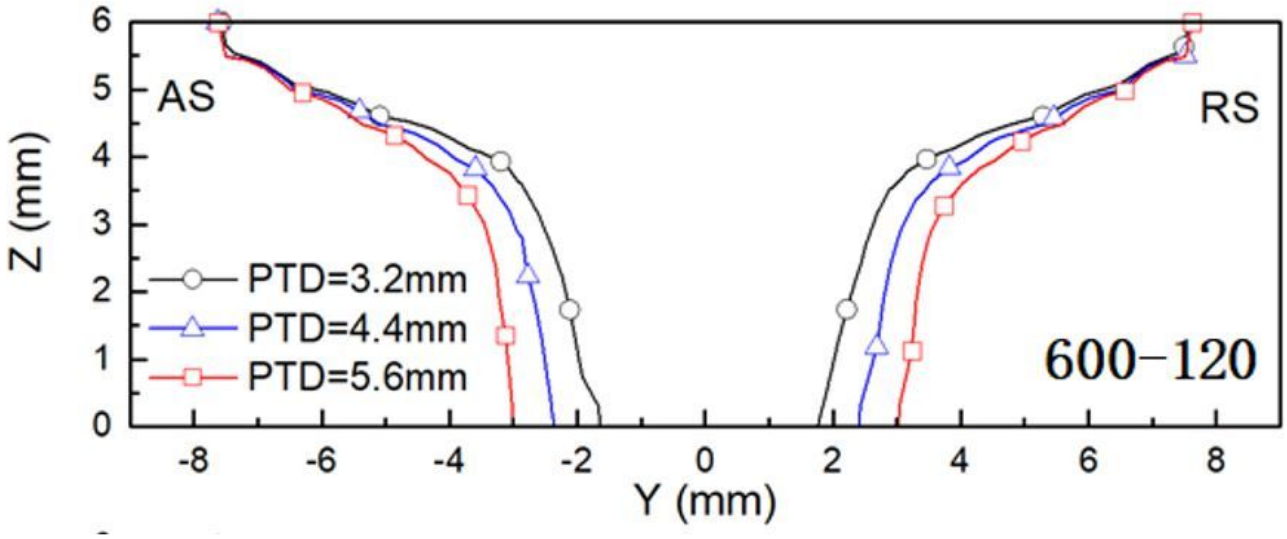

Figure 13

Comparison of TMAZ boundaries for different pin tip diameters.

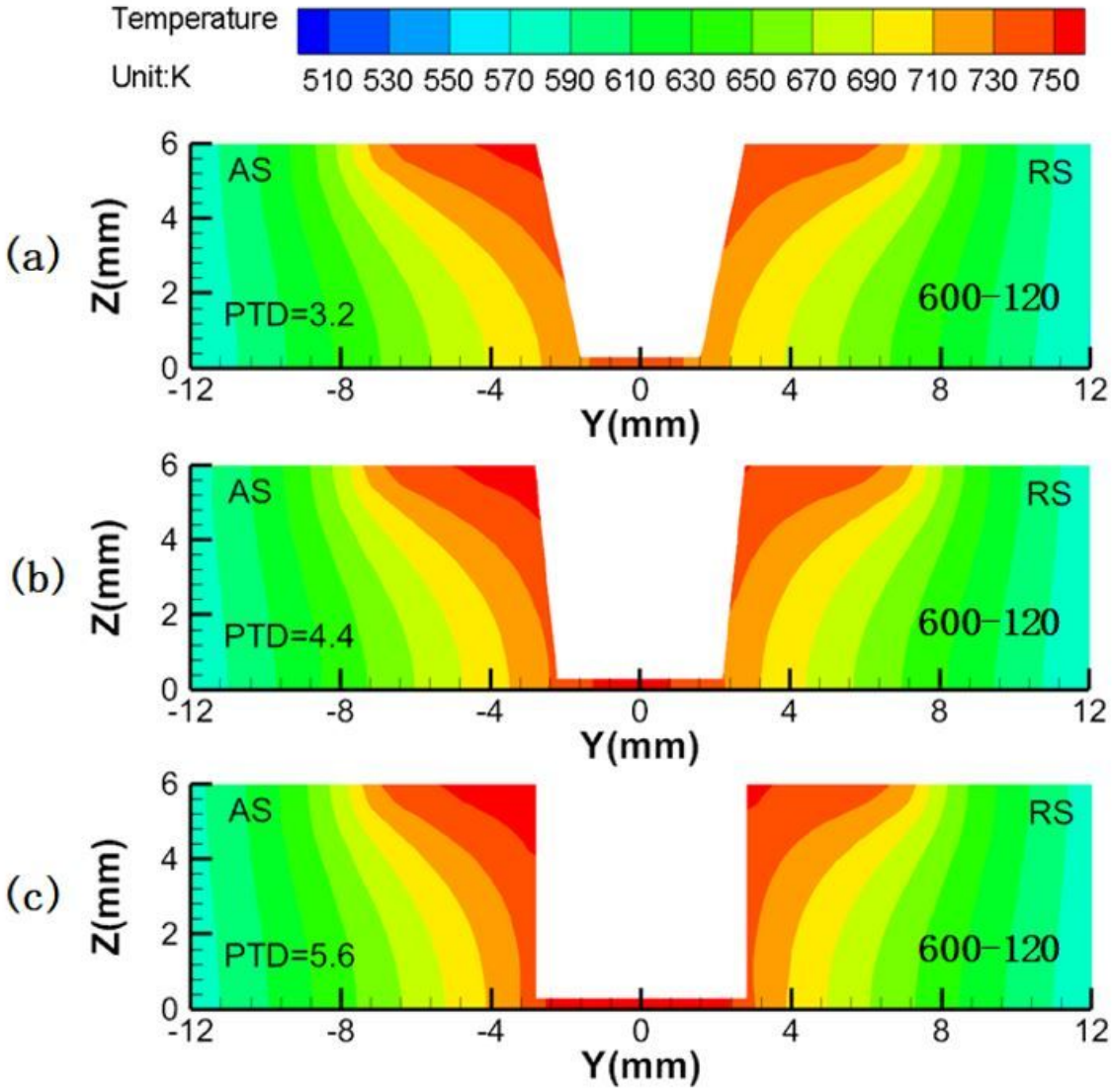

Figure 14

Comparison of temperature fields at transverse cross-section for different pin tip diameters.

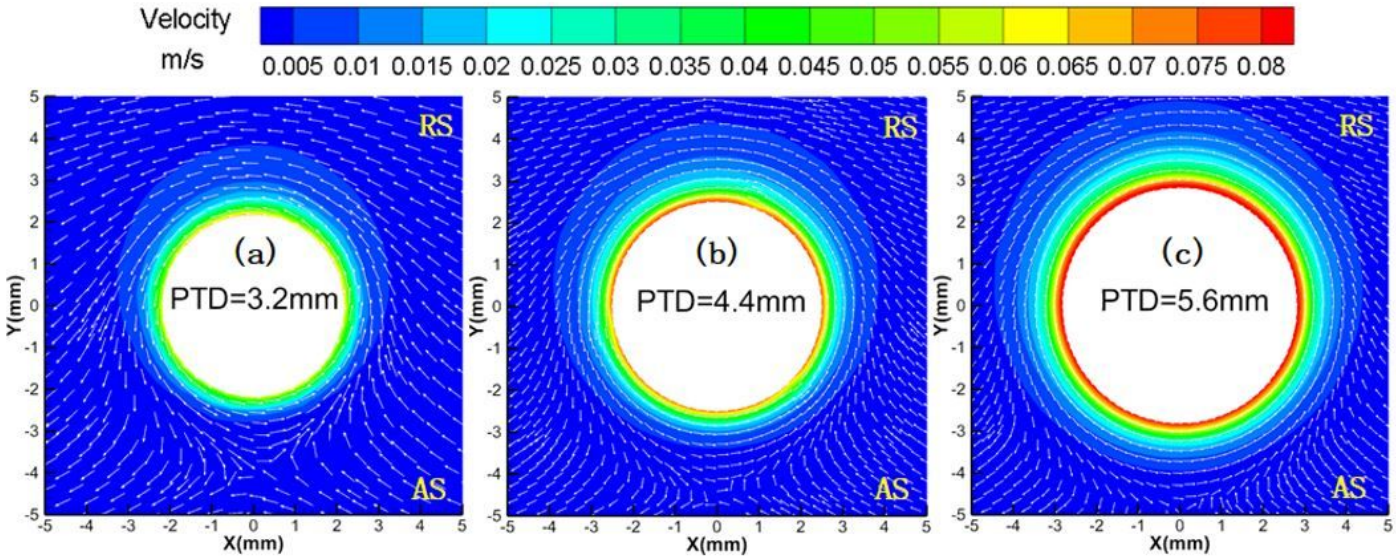

Figure 15

Comparisons of velocity contours and vectors at z = 3mm horizontal plane for different pin tip diameters.

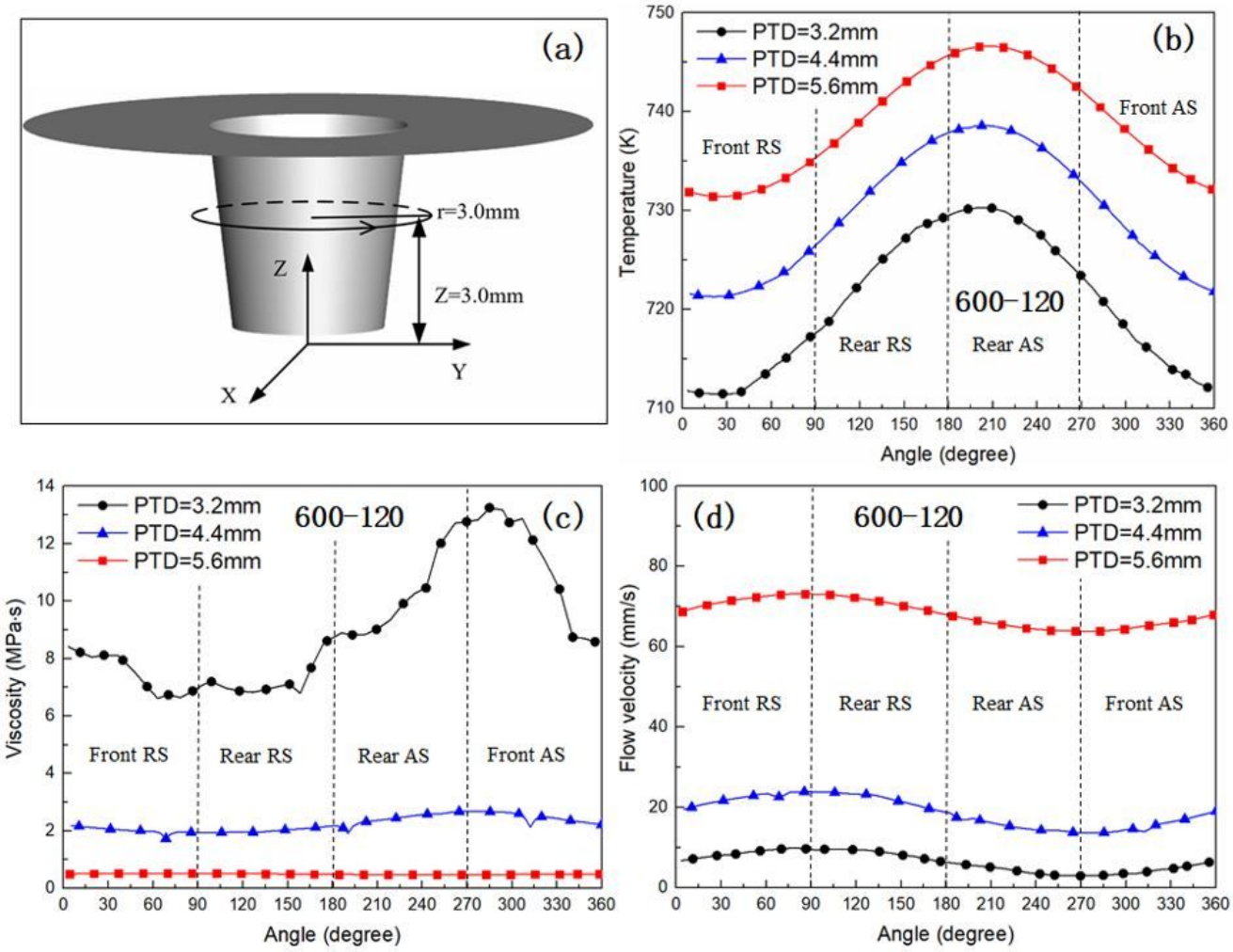

Figure 16

(a) Schematic drawing of the location at z = 3 mm and r = 3 mm. Variation curves of the (b) temperature, (c) viscosity, and (d) flow velocity for different pin tip diameters at the location.

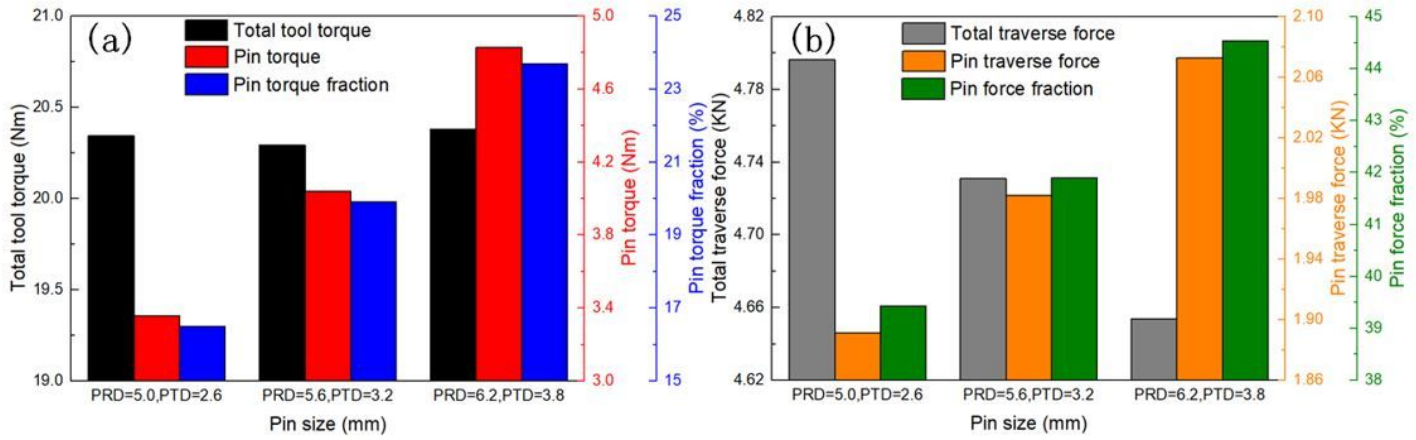

Figure 17

Comparison of (a) torque and (b) transverse force for different pin sizes.

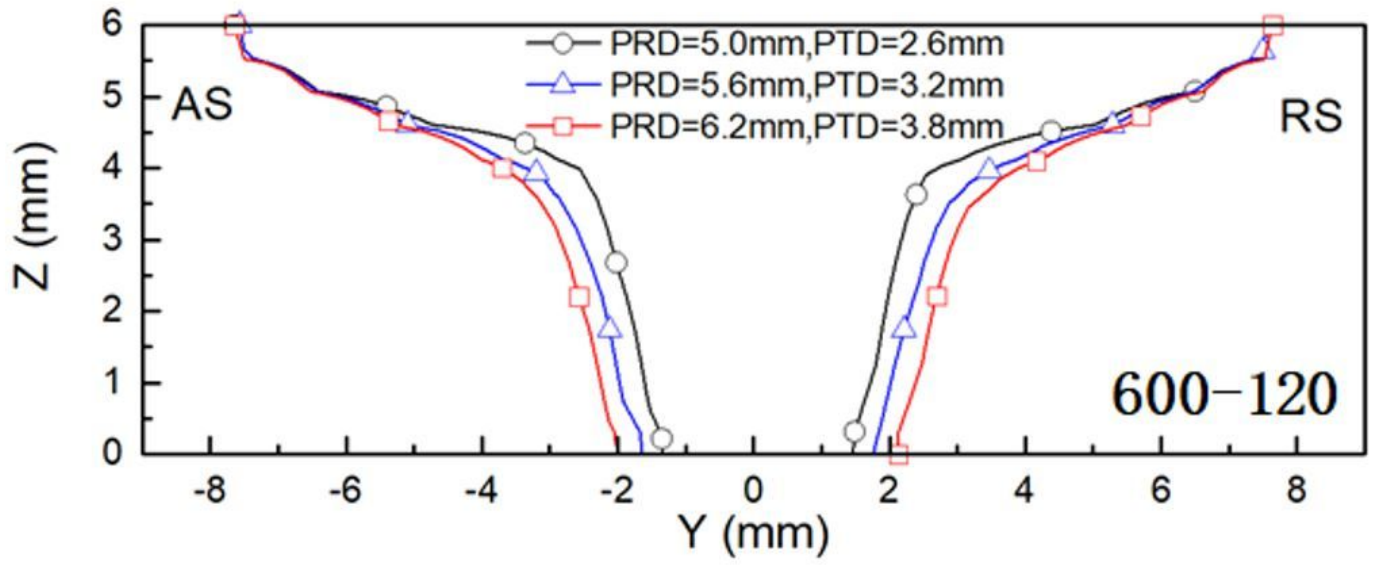

Figure 18

Comparison of TMAZ boundaries for different pin sizes.

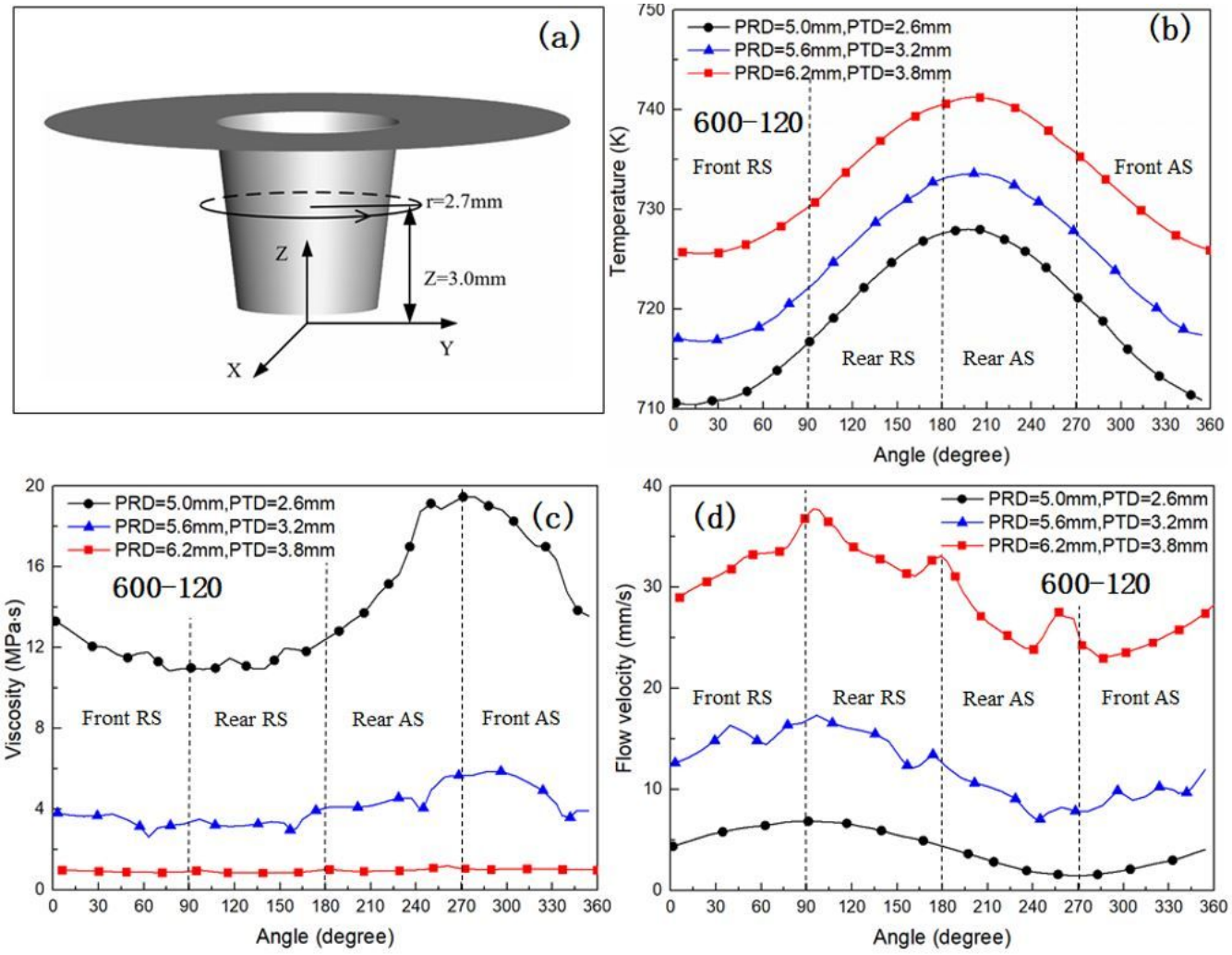

Figure 19

(a) Schematic drawing of the location at z = 3 mm and r = 2.7 mm. Variation curves of the (b) temperature, (c) viscosity, and (d) flow velocity for different pin size at the location.